The core-shell nanowire as a solar cell

A graduation capstone thesis in partial fulfillment of the requirements for the degree of Bachelor of Science

Submitted by
Kim Dinh Hoang, John
AUC Student Number: 10234985

29 May 2014

Submitted to
Supervisor: Dr. Forrest R. Bradbury
Reader: Dr. Jan Pieter van der Schaar
Word count: 9980

Layman's Summary

The increase in global electricity consumption, together with the concerns over climate change, has drawn research attention to new sources of renewable energy. One of the renewable energy technologies is photovoltaics (PV), which uses the sun as an abundant energy source. The most common photovoltaic material currently used for solar cell devices is Silicon. However, Silicon cannot absorb all photons coming from the sun, and there is an efficiency limit of 33% for a single junction silicon solar cell device. This thesis investigates an alternative photovoltaic material for Silicon, namely, the nanowire.

The nanowire is a wire that is several hundred times smaller than a human hair. Its small size gives rise to interesting properties, particularly its ability to absorb really well photon from the sun. By wrapping a thin layer of semiconducting material around the nanowire, the nanowire's absorption efficiency can be enhanced even further. On the other hand, the nanowire's small size also makes it difficult to handle, and special methods must be used to electrically characterize a nanowire, as well as to turn a nanowire into a complete working nanoscale solar cell device. Specifically in this project, in order to electrically characterize the nanowire, Photolithography is used to build a nanostructure that connects two ends of the nanowire with measurement devices. After the characterization has been done, we use another method of lithography, namely, Electron Beam Lithography, to build a complete nanoscale solar cell device. We attempt to extract the power conversion efficiency of the solar cell device, but the data is inconsistent and no sensible information could be obtained. In the future, optimization of Electron Beam Lithography process should be carried out in order to determine accurately the power conversion efficiency of our nanoscale solar cell device, and we also suggest further investigation on the contact surface to explain several anomalous observations from the electrical characterization.

Abstract

This project investigates on how a core-shell nanowire can be used as a building block for a solar cell device. With the formalism proposed by [1] and [5], we review the solutions to Maxwell's equations that describe the interaction between an incident electromagnetic plane wave and an infinitely long cylinder, known as Mie Theory. With Mie Theory as a basis, we review the numerical results from Mann et al. [2] that demonstrate the enhanced light absorption of core-shell nanowire structure relative to the solid nanowire structure. Next, we use Photolithography to fabricate metal contacts on the shell of the $Ag@Cu_2O$ core-shell nanowire in order to perform electrical characterization on the wire. The saturation current, ideality factor and barrier height are found to be $2.2\,\mu A$, 15, and 0.24 eV, respectively. Next, we use Electron Beam Lithography to build a nanoscale solar cell device which consists of an $Ag@Cu_2O$ core-shell nanowire with a Schottky contact on the Cu_2O shell and a metal contact on the silver core. Finally, we attempt to extract power conversion efficiency of this nanoscale solar cell device by analyzing its Current-Voltage characteristic graph. The results are not consistent and no sensible information could be obtained at the writing point of this thesis. Possible future studies include the optimization of Electron Beam Lithography process and better understanding of surface properties.

Keywords: electrical characterization, lithography, Mie Theory, nanowire, nanotechnology, optimization, photovoltaic, solar cell, semiconductor.

List of Figures

Acknowledgements

En God zei: Laat er licht zijn. En er was licht. (Genesis 1:3–4)

Everything started with Stephen Helms' suggestion after a Sunday Mass that finally convinced me to join the group Nanoscale Solar Cell at AMOLF. It has brought me on a memorable journey, the fruit of which is this graduation thesis. I would like to thank Erik Garnett for letting me be a part of his group at AMOLF, Sebastian Oener for teaching me the intricate art of photolithography (and for tolerating my absent-mindedness from time to time), and finally, Forrest Bradbury for the much-needed guidance and encouragements during difficult time. To all my supervisors, thank you for guiding me on this exciting field of photovoltaic materials. A special thank goes to Forrest for being a very amazing mentor and friend.

Most of my works would not have been the same without the knowledge and collaboration from Beniamino and Sander. I appreciate the intellectually engaging conversations that we had, and thank you for clarifying difficult concepts that I encountered along the way. I am looking forward to working with you again in the future.

Felipe, Abbas were my wonderful lab-mates who made my hours in the clean room much more fun and easier. Thanks for the advices and tips that saved me from many troubles from time to time. To the technicians Dimitry, Hans, thanks for providing me with necessary trainings, as well as for keeping cleanroom's machinery safely humming and running.

Last but not least, to my parents, sister and Ivy, for waiting patiently for me during my long working hours in the lab, for always being there for me when I'm in need, and for all your supports.

Content

1 Introduction

The increase in global electricity consumption, together with the concerns over climate change, has drawn research attention to new sources of renewable energy. One of such renewable energy technologies is photovoltaics (PV), which uses the sun as an abundant energy source. In recent years, extensive research on photovoltaic (PV) materials has shown promising examples. Currently, silicon solar cells have been able to demonstrate high power conversion efficiencies up to 25% [3]. However, silicon solar cells suffer from high energy costs, since manufacturing high efficiency silicon solar cells requires extensive purification processes which are costly and have low throughput. Furthermore, the efficiency of a single p-n junction silicon solar cell is limited by Shockley–Queisser limit (Figure 1.1), which imposes the maximum theoretical efficiency of the cell that depends on the material's particular bandgap. This limit can be surpassed using multijunction cells, at the cost of increasing complexity. It is clear that in order for solar electricity to be cost-effective and competitive, improvements must be made not only in energy conversion efficiency but also in manufacturing processes, especially in terms of throughput and material usage.
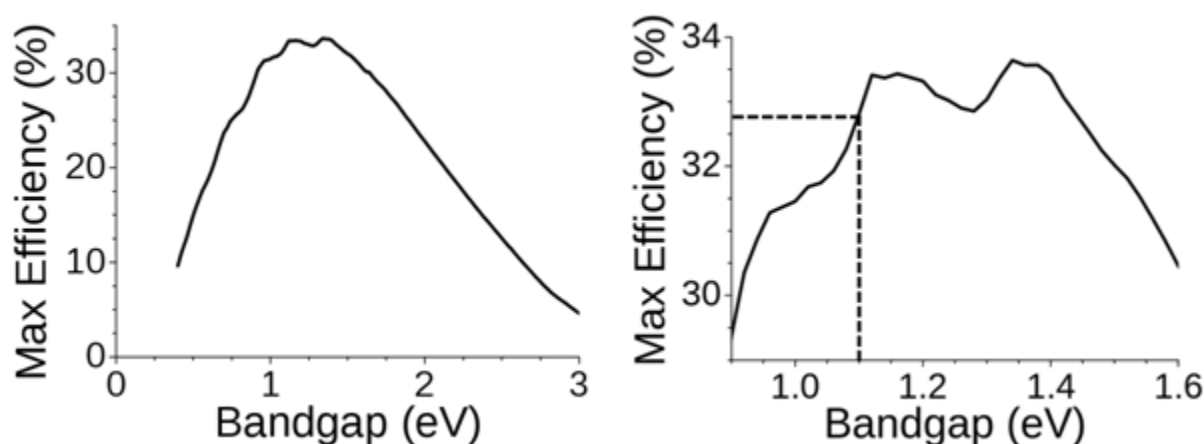
Figure 1.1: Shockley–Queisser limit for a single p-n junction solar cell. Right: blown-up region near the peak. The most popular material for solar cell, silicon, has a bandgap of 1.1eV and thus a maximum efficiency of about 33%. Image obtained from [8].

New materials have been proposed as candidates for new generation of solar cell, and they are categorized as "emerging PV" in figure 1.2. Research on emerging PV materials such as quantum dots, dye-sensitized cells, etc is still in its early stage but has already shown promising results. From figure 1.2, one can observe qualitatively that, on the time-horizon over the most recent decade (2005-2015), the increase in efficiency of these emerging PV materials (red solid trend lines, lower right corner) has been the most rapid. It is possible that these emerging PV materials will surpass today's most efficient solar cells in the near future. The nanowire is one of these materials, and possesses several desirable properties for an efficient solar cell.

Figure 1.2: Progress on developments of different types of solar cells [9].

For an effective solar cell, thick semiconductor layers are needed to absorb all of the above bandgap photons, while thin layers are preferred to efficiently extract charge carriers by minimizing the distance to the metal contacts and thereby preventing charge recombination. An ideal solar cell therefore has to achieve seemingly contradictory requirements: near unity absorption in thin layers. Metal-semiconductor nanowires show themselves to be a prom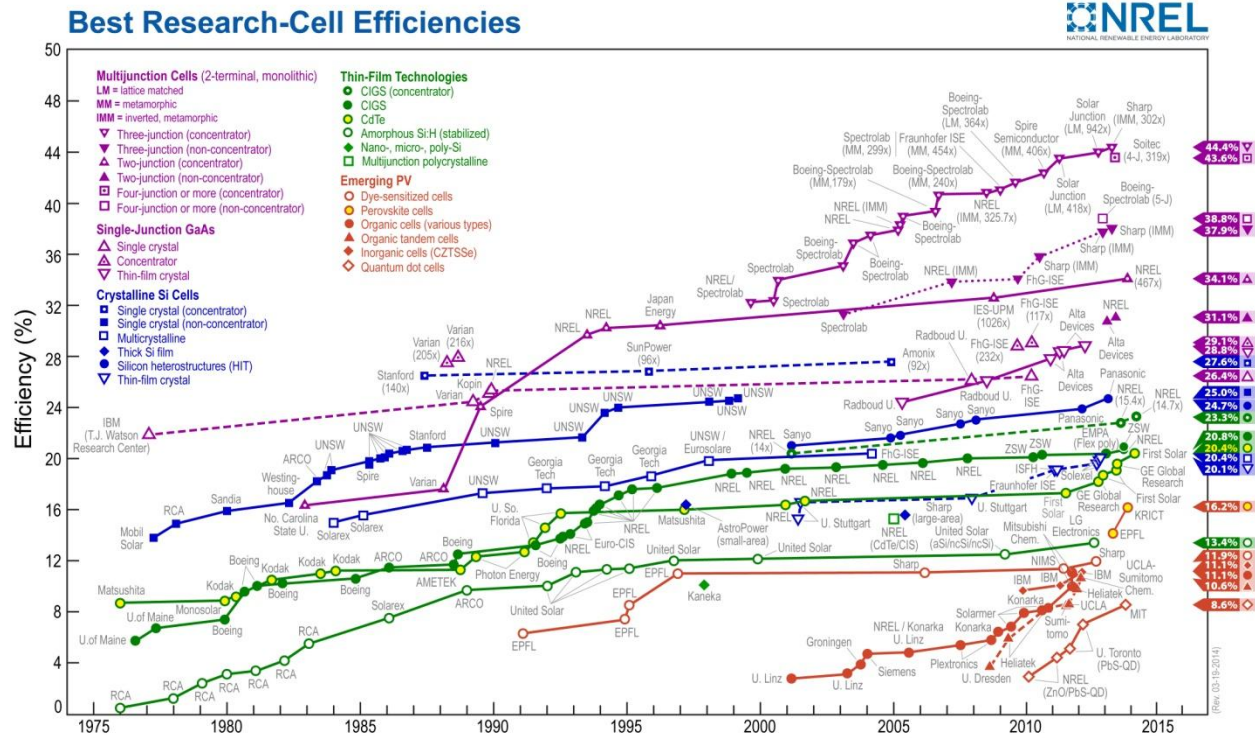ising candidate for next generation solar cells because of their their tunable photon absorption, in addition to the potential for low cost production. Tsakalakos et al. [12] reported a nanowire-based solar cell on metal substrates with efficiency of 0.1%. From another research group, arrays of silicon nanowires have been integrated into solar cells with an energy conversion efficiency of 1.9 % [11]. Recently, it has been suggested [4] that inserting a metal nanowire into an ultrathin semiconductor shell (hybrid core-shell coaxial geometry) can improve the efficiency by further enhancing photon absorption. Numerical simulation shows that this a hybrid coaxial nanowire geometry can indeed outperform solid semiconducting nanowires while reducing significantly the semiconductor bulk volume [2]. Experimentally, Tang et al. demonstrated that a CdS@Cu_2S (CdS core and Cu_2S shell) has achieved an energy conversion efficiency of 5.4%, which is "superior to those reported for equivalent planar cells" [3]. Such core-shell nanowire structure can be the building blocks for photovoltaic materials.

In this project, we first reviewed the background theory and literature behind the enhanced photon absorption of a core-shell nanowire as well as the basic operating principles of a semiconducting solar cell device, namely, Mie Theory and Band Theory. Next, instead of using

2

CdS and Cu_2S as previously reported in [13], we used another common semiconducting material Cu_2O and the metal Ag for the nanoscale solar cell device, since these materials have not been reported in literature before (at least prior to the start of this project). We then fabricated a device consisting of an Ag@Cu_2O core-shell nanowire, a Schottky (rectifying) contact, and an Ohmic (non-rectifying) contact using Electron Beam Lithography (EBL). We then attempted to extract several important parameters that characterized the device through an analysis on the current-voltage graph, and discussed their implications for the potential power conversion efficiency of core-shell nanowire solar cells.

2 Literature review and background theory

This section reviews three theories underlining the basic operating principles of the core-shell nanowire as an operational solar cell device, namely Mie Theory, Metal-semiconductor junctions and Schottky diode equation. Mie Theory (2.1) motivates the use of core-shell nanowire structure. Band Theory (2.2) used in metal-semiconductor junction provides a microscopic view of the charge dynamics inside the device, while Schottky diode equation describes macroscopically the electronic properties of the device. Section 2.3 also introduces several important parameters that will be used to evaluate the experimental results in the later part of this thesis.

2.1 Mie Theory

Nanowires are often treated as infinitely long cylinders to approximate the analytical description of the interaction between incoming photon and the nanowire. The description can be done using Mie Theory, which refers to the solutions of Maxwell's equations in a scattering problem that provide the incident, scattered and internal fields of a sphere or an infinitely long cylinder. These solutions are written analytically in the form of an infinite series expansion from which various optical properties (intensity distribution, optical cross-section, absorption efficiency, etc) of a nanowire can be studied. Section 2.1 reviews the Mie formalism that demonstrates theoretically the enhanced absorption in core-shell structure which can be used as a building block for the photovoltaic device. It starts with the generic description of the scattering problem and provides the solutions, together with the descriptions of "Mie modes" inside the nanowire. It next demonstrates the high weighted absorption efficiency of a solid nanowire, and how this efficiency can be overcome using a core-shell structure.

In the simplest terms, the scattering problem is posed as follows: Assume that one has an infinitely long metal cylinder and a polarized incoming wave incident at an angle θ to the cylinder's normal axis. Part of the wave is reflected off the cylinder's surface (scattered wave) while another part is absorbed into the cylinder (internal wave) (figure 3.1). How do the electric and magnetic fields of the scattered and internal waves depend on the incident angle θ and the cylinder's radius R?
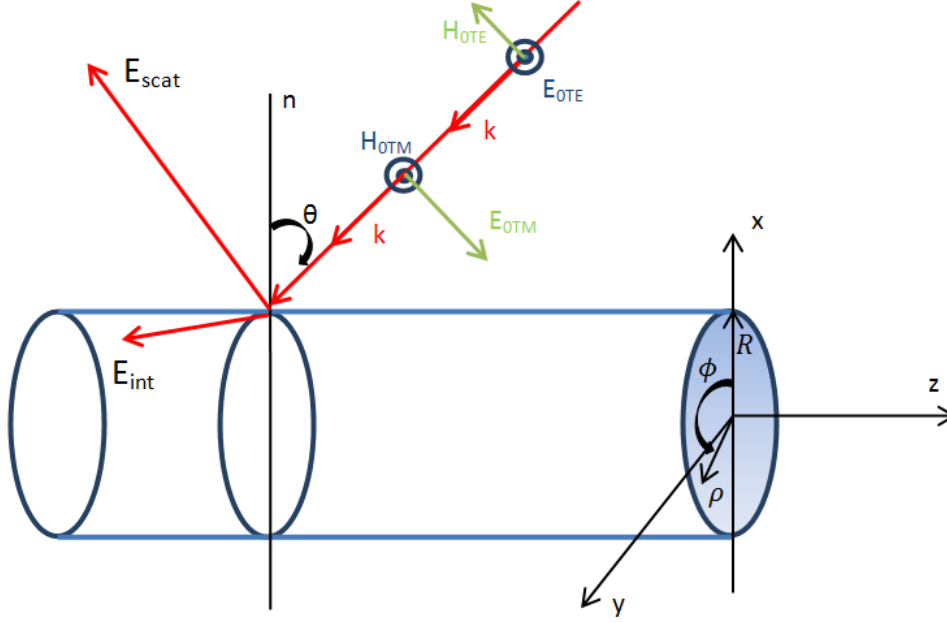
Figure 2.1: Coordinates for the scattering problem. The polarized incoming wave with the incident angle θ is shown. Note that the polarized incoming wave is resolved into two components (or modes): Transverse Magnetic Mode (TM mode) where the magnetic field of the incident wave is normal to the cylinder axis and Transverse Electric Mode (TE mode) where electric field of the incident wave is normal to the cylinder axis. Figure adapted from [1].

The electric and magnetic fields of the absorbed and scattered waves can be solved by imposing appropriate boundary conditions while solving the vector wave equation for electromagnetic fields in the absence of free charge. The expression for the fields inside the cylinder (absorbed wave) can be obtained. The behaviors of electromagnetic waves propagating inside the cylinder are particularly interesting. In the case of nanowires having dimension on the order of magnitude of the wavelength, the boundary conditions impose a restriction on the number of modes available, which gives rise to the discrete spectrum of eigenmodes. This is in contrast to the case of unconstrained media such as vacuum or bulk materials when the spectrum of modes available for light propagation is continuous. The situation is analogous to quantum wells, when a reduction in size (quantum confinement) leads to the emergence of discrete states.

For the absorbed wave, by imposing the boundary conditions to the fields at the cylinder's surface, we obtain the following equation [5]:

$$\left[\frac{\mu_{int}}{lR}\frac{J_n^{'}(lR)}{J_n(lR)} - \frac{\mu_{ext}}{jR}\frac{H_n^{'}(jR)}{H_n(jR)}\right]\left[\frac{\epsilon_{int}}{lR}\frac{J_n^{'}(lR)}{J_n(lR)} - \frac{\epsilon_{ext}}{jR}\frac{H_n^{'}(jR)}{H_n(jR)}\right] = \pm n^2\left(\frac{k_z}{k_0}\right)^2\left(\frac{1}{(jR)^2} - \frac{1}{(lR)^2}\right)^2 \quad (2.1)$$

In this equation, $l \equiv k_0 cos\theta$, J and H are Bessel and Hankel functions of the fist kind, apostrophe denotes first derivative. The integer n is their order, which also denotes the *azimuthal* mode number that describes the number of field maxima in the azimuthal (ϕ) direction. $k_o =$

$2\pi/\lambda$ is the free wave number, $k_z = 2\pi/\lambda_{eff}$ is the effective wavelength of the mode propagating inside the nanowire. μ and ε denote the permeability and permittivity of the internal (int) and external (ext) media. In the simplest case of ($n=0$), the right hand side of the equation vanishes. We can separate the left hand side of equation 2.1 into two equations that describe either pure TM or TE modes (signatures):

$$\frac{\mu_{int}}{lR}\frac{J_n'(lR)}{J_n(lR)} - \frac{\mu_{ext}}{jR}\frac{H_n'(jR)}{H_n(jR)} = 0 \text{ for TE}_0 \text{ modes (2.2a)}$$

$$\frac{\epsilon_{int}}{lR}\frac{J_n'(lR)}{J_n(lR)} - \frac{\epsilon_{ext}}{jR}\frac{H_n'(jR)}{H_n(jR)} = 0 \text{ for TM}_0 \text{ modes (2.2b)}$$

In order to solve the two differential equations above, we need to introduce an additional quantum number κ that denotes the *radial* mode number (also the number of field maxima in the radial (ρ) direction). Together this pair of quantum numbers (n,κ) gives the complete description of the wave number k_z inside the cylinder. This wave number can be associated with the effective wavelength of a mode propagating inside the cylinder: $k_z=2\pi/\lambda_{effective}$.

In the case of cross mode ($n \neq 0$), the differential equation 2.1 is harder to solve, and the signature is neither purely TE nor TM. Conventionally, the magnetoelectric modes (HE modes) are obtained by taking the '+' sign on the right hand side of the equation, while the electromagnetic modes (EH modes) appear when the '-'sign is taken. The electric field profiles of the first few modes are given in figure 2.2. Qualitatively, the profiles of the cross modes resemble the so-called whispering gallery modes. In the case of large azimuthal mode (large *n*), the electric field of the modes is confined in the region near the circumference of the cylinder's cross section, similar to sound traveling in a whispering gallery (figure 2.2).
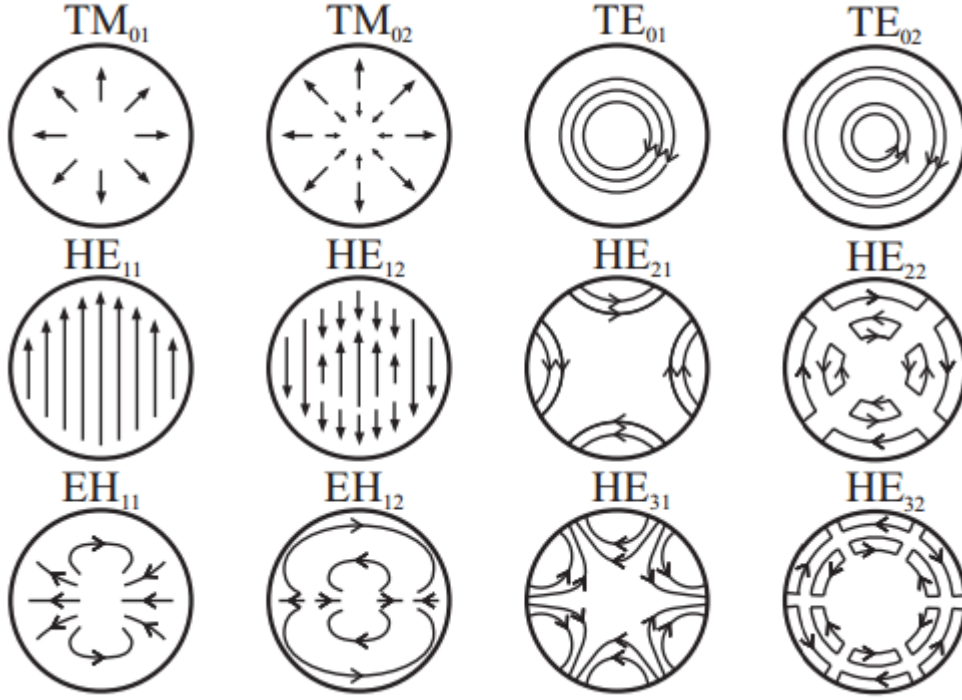
Figure 2.2: Plot of the electric field lines of low-order Mie modes at the cross section of an infinitely long cylinder [5]. Notice the "whispering gallery" modes HE_{22} and HE_{32} with the electric field circling near the wire's circumference.

Similarly, we can obtain the fields outside the nanowire. Due to space constraint, we provide the expression for the fields in Appendix A. Roughly, the scattered electric and magnetic fields are given as an infinite sum of cylindrical harmonics, which involve seven coefficients, each of which depends on the cylinder's radius R, the scattering angles θ and the wave number k of the incoming wave. Undoubtedly, even though Mie solutions have been worked out analytically, numerical simulation proves to be a more practical approach. Interested reader can find more details in [1] or in Appendix A.

Next, having obtained the fields inside and outside the cylinder, it is now possible to study the absorption and scattering efficiency of the cylinder. Figure 2.3 provides the color plot of absorption efficiency as a function of incoming wavelength and nanowire diameter. The figure also shows a broadband of relative high absorption efficiency in the visible spectrum (450 to 700 nm).
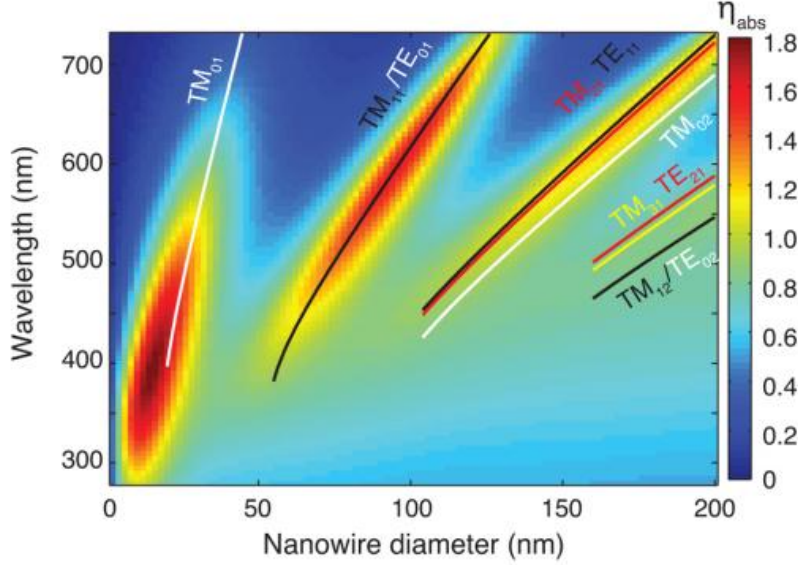
Figure 2.3: Absorption efficiency as a function of wire diameter and incident wavelength [2]. Notice in figure 2.3 that for higher order modes, the absorption efficiency is relatively low as compared to the TM_{01} mode, and when the wavelength is below 400, the wires hardly absorb TE modes. Notice that the absorption coefficient η can be greater than unity due to the fact that nanowires can have an optical cross section exceeding their geometrical cross section.

From figure 2.3, it can be seen that we can obtain a maximum absorption efficiency of 1.8 if the nanowire has a diameter of 15nm and the incoming wavelength is around 380nm. For any given nanowire diameter, there is a particular incoming wavelength at which the absorption efficiency is maximized. Physically, this situation is called critical coupling: the phase and amplitude of the incident and scattered waves are matched such that they yield complete destructive interference, which leads to the highest energy resonance inside the cylinder and hence to the maximum absorption cross section [2]. However, in photovoltaic materials, broadband absorption is preferred, and an efficient solar cell must absorb well across all incoming photon wavelengths from the sun. As such, an optimization of absorption efficiency must be done over the entire solar spectrum. Therefore, we define next the weighted absorption efficiency, which measures the total number of photons absorbed in a single nanowire relative to the total photon flux through the wire's geometrical cross section. For a given wire diameter, the weighted absorption efficiency is given by:

$$\langle \eta_{abs} \rangle_{AM1.5}(R) = \frac{\int \eta_{abs}\, F_s(\lambda)d\lambda}{\int F_S(\lambda)d\lambda} \ (2.3)$$

where $F_S(\lambda)$ is the photon flux density in the AM1.5 solar spectrum. The plot of weighted absorption efficiency as a function of nanowire diameter for different modes is given in figure 2.4. For unpolarized incoming wave, a maximum weighted absorption efficiency of 0.9 is obtained at diameter of 110 nm.
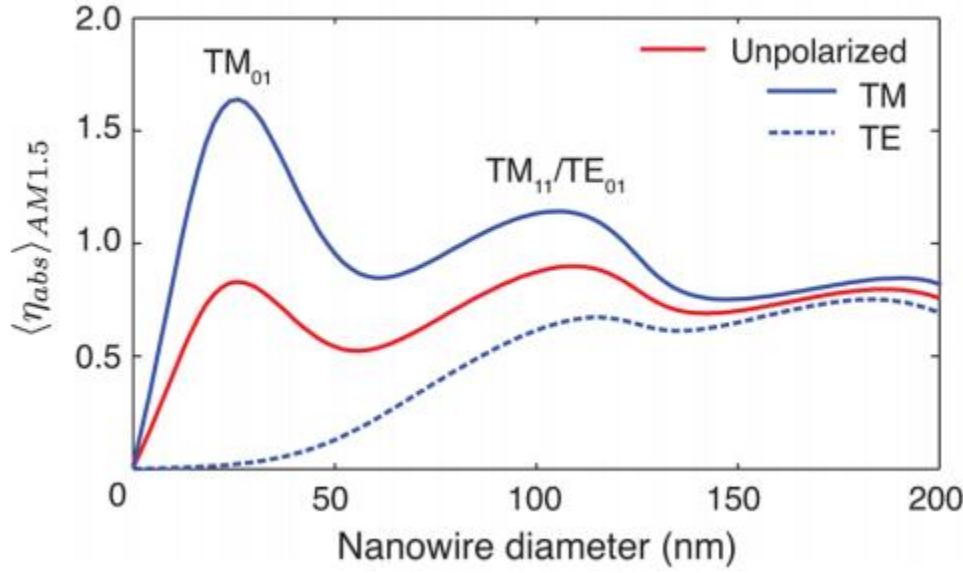
Figure 2.4: Weighted absorption efficiency when the incident light is unpolarized (red), in TM mode (solid blue) and in TE mode (dashed blue) as a function of the diameter [2].The peaks of TM correspond to critical coupling (with the modes labeled above each peak).

However, the maximum absorption efficiency can be increased further by wrapping a thin layer of semiconducting material around the nanowire. By changing the integration limit in the definition of absorption efficiency, we can model the absorption in the core-shell structure. The plot of weighted absorption efficiency of the shell as a function of shell thickness for different modes is given in figure 2.5, which demonstrates the enhancement in the weighted absorption efficiency.
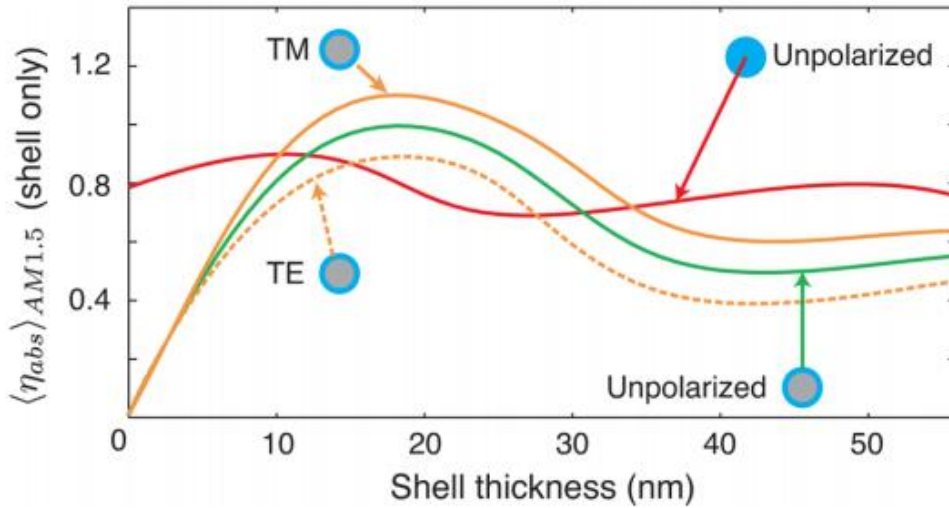

Figure 2.5: Weighted absorption efficiency in a core-shell structure with varying shell thickness. The core is 88nm in diameter.

In figure 2.5, red solid line is the weighted absorption efficiency of a solid semiconducting nanowire, and green solid line is the weighted absorption efficiency of a core-shell nanowire. For unpolarized incoming wave, the maximum absorption of core-shell wire geometry is unity, which is higher than the maximum absorption of solid wire geometry despite using less semiconducting material. The red solid line does not start from the origin because it is wrapping around a core with 88 nm diameter.

To summarize, section 2.1 has provided a coherent theoretical landscape that motivates the use of core-shell nanowires as the building block for photovoltaic devices. Starting from the formalism of Mie Theory and the scattering problem, we review the definition of several important parameters (optical cross section, Mie modes). Next, we demonstrate the fundamental limit of the optical cross section of a solid nanowire. Finally, with the results in [2], we review how the nanowires with core-shell geometry improve the photon absorption efficiency.

2.2   Band Theory: Metal-Semiconductor junctions

Next, we assume that the photon energy that has been maximally absorbed in a core-shell nanowire is stored as an oscillating electric field. The field can excite the electrons inside the nanowire, which must be extracted in order to generate a photocurrent. Specifically, the electric field stored inside the nanowire can generate electron-hole pairs. Ideally, the electrons must be separated from the holes to drive the current to the load and to minimize charge recombination which results in energy loss. In a functional solar cell device, the nanowire can be considered macroscopically as a current generator that drives electrons only to the load. The flow of the photocurrent can be controlled via metal-semiconductor junctions if they have rectifying properties similar to p-n junction in semiconductor diodes. By forming appropriate contacts (junctions) at two ends of the wire, the contact can be made either rectifying (Schottky) or non-rectifying (Ohmic). A device architecture with unidirectional flow of charge carriers can be realized according to figure 2.6.

10
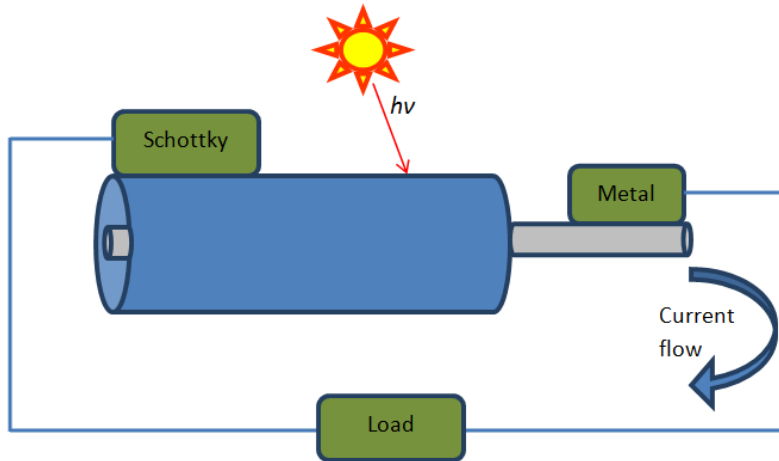
Figure 2.6: Schottky and Ohmic contacts on the core-shell nanowire architecture to ensure directional current flow to the load. The shell of the nanowire is made of semiconducting material. The Schottky contact is on the shell, while the Ohmic contact is between the shell and the core of the nanowire.

A Schottky contact refers to the junction between a metal and a semiconductor that allows charge carriers to flow only in one direction, similar to a p-n junction in diodes. As such, we attempt to explain the concept using Band Theory. We assume in this section that the semiconductor is p-type, and ignore Fermi-level pinning for now. The band diagram of the metal-semiconductor contact is depicted in figure 2.7.

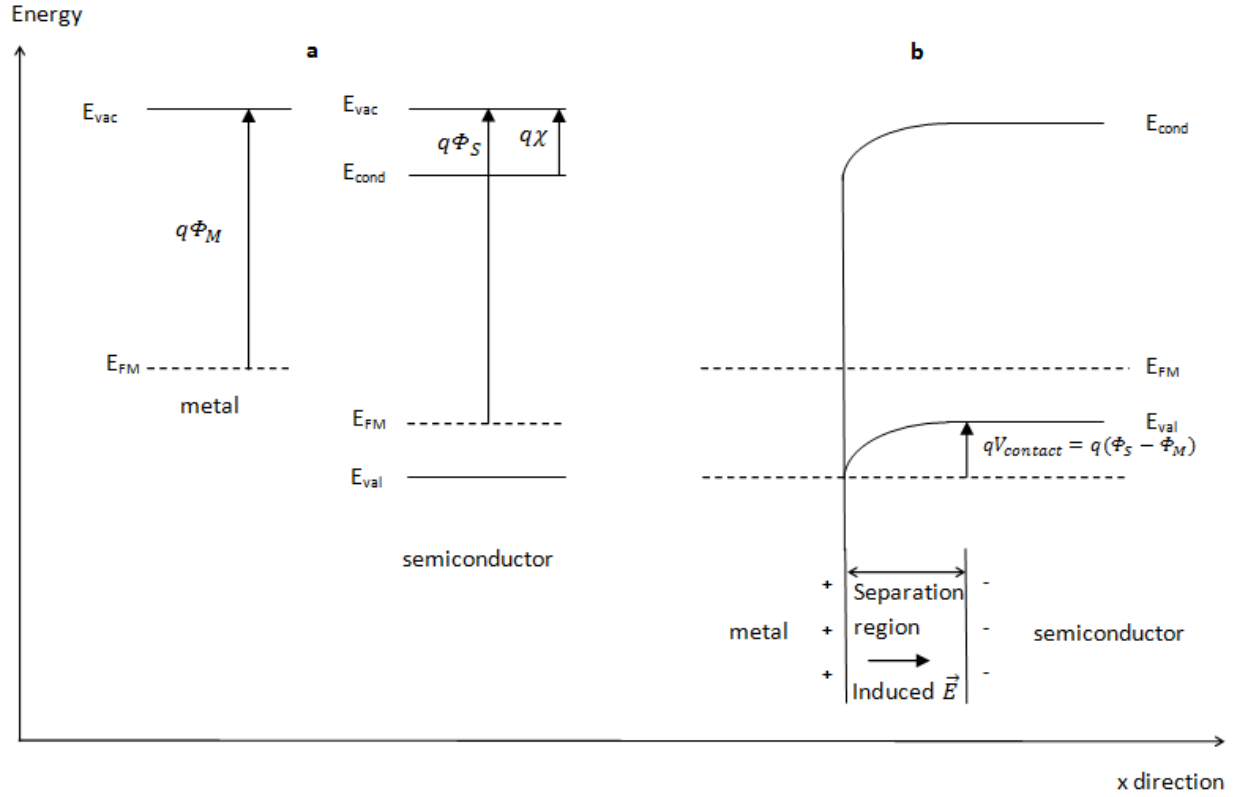Figure 2.7: Band diagram for metal-semiconductor (p-type) Schottky junction before contacting (a) and after equilibrium (b).

In the diagram, $q\Phi_M$ ($q\Phi_S$) is the work function of the metal (semiconductor), which is the energy required to remove an electron from the Fermi level to the vacuum outside the metal (semiconductor), $q\chi$ is the electron affinity of the semiconductor, which measures the energy required to remove an electron from the conduction band minimum to the vacuum outside the semiconductor. The work function of the metal is larger than that of the semiconductor.

After the metal and the semiconductor are brought in contact, electrons flow from the metal to the semiconductor, bending the band energies to align the Fermi levels until equilibrium is established. When equilibrium has been achieved, a charge accumulation region is formed in the region between the metal and the semiconductor interface (Figure 2.7b). The negative charges (electrons) on the metal due to charge migration are matched with the positive charges (holes) on the semiconductor. This charge separation induces an electric field in the accumulation region, which is usually expressed in terms of contact potential ($V_{contact}$ in figure 2.7). The high contact potential generates a barrier that prevents additional electrons from diffusing from the metal, and is measured as $q(\Phi_S - \Phi_M)$. By applying either forward or reverse bias, the potential barrier can be lowered or raised accordingly.

Unlike Schottky contact, an Ohmic contact is defined as the junction between a metal and a semiconductor in which there is an unimpeded transfer of charge carriers from one material to another. The band diagram of an Ohmic metal-semiconductor contact is depicted in figure 2.8.
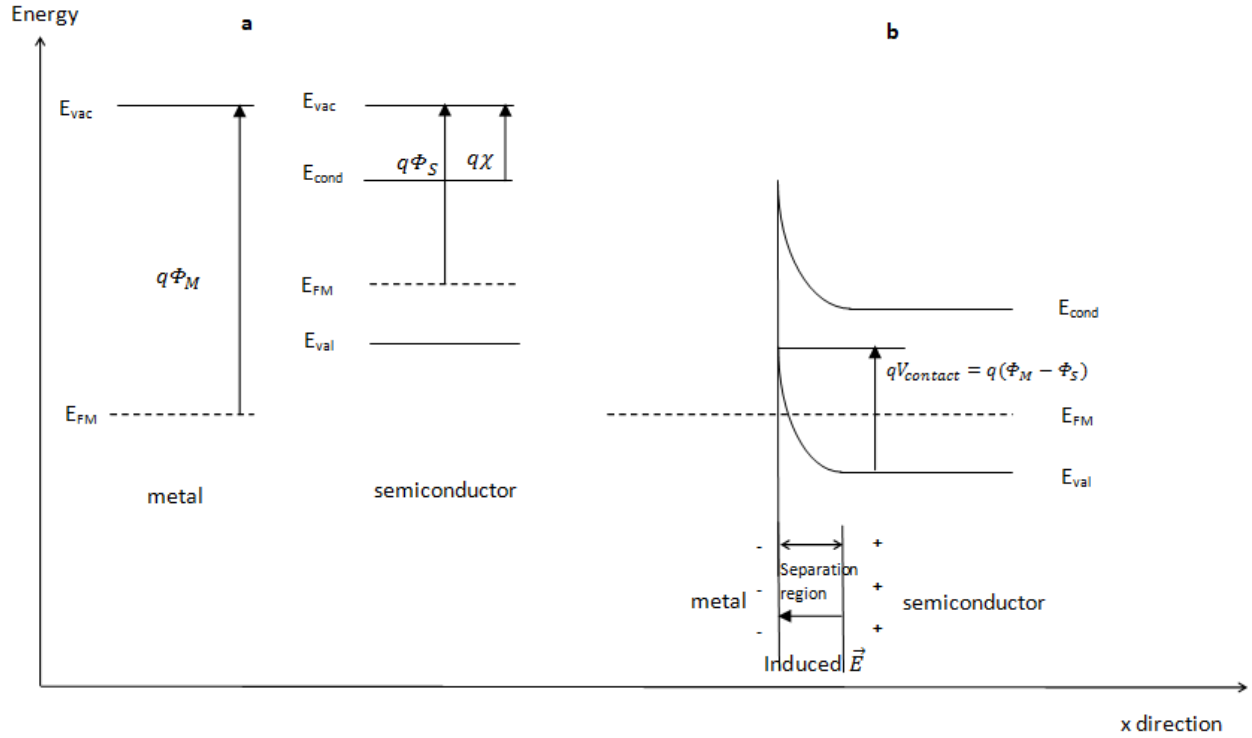

Figure 2.8: Band diagram for metal and semiconductor (p-type) Ohmic junction before contacting (a) and after equilibrium (b).

Similar to Schottky junction, after the metal and the semiconductor are brought in contact, electrons flow from the semiconductor to the metal, bending the band energies to align the Fermi levels until equilibrium is established. After equilibrium has been achieved, a charge accumulation region is formed in the region between the metal and the semiconductor interface (Figure 2.8b). In reality, Schottky and Ohmic contacts are also dependent on the major charge carrier type of the semiconductor. The band diagrams in this section work with p-type semiconductor since the material of the shell of the nanowire used in experiments is Cu_2O.

According to figure 2.7, the semiconducting shell forms a Schottky contact with the metal contact outside the shell, and an Ohmic contact with the core inside the nanowire. The combined band diagram for such scheme is given in figure 2.9. Electrons inside the shell are excited to the conduction band, separating the positively charge holes and negatively charges electrons. The excited electrons flow to lower potential region in the metal contact on the left. The situation is reversed for the positively charged holes, which flow to the core on the right instead.
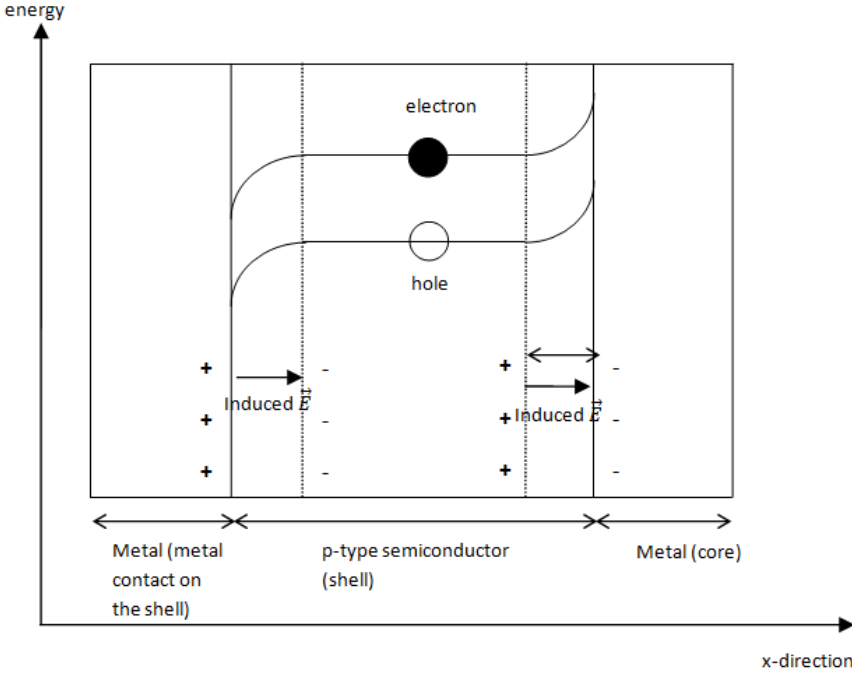
13

Figure 2.9: Combined band diagram according to the complete nanowire solar cell device architecture as depicted in figure 2.6. The p-type semiconductor is "sandwiched" between two layers of metals, with a Schottky metal contact on the left of the semiconductor and an Ohmic contact on the right of the semiconductor. The electron is excited to the conduction band inside the semiconductor, leaving a positive hole.

2.3 Schottky Diode Equation

Given the fact that the rectifying property of a Schottky metal-semiconductor junction is similar to that of a p-n junction, and assuming further that the Ohmic contact is ideal with negligible voltage drop across the junction, we can expect the Current-Voltage (*I-V*) characteristic of the solar cell device in figure 2.6 to behave according to the diode equation:

$$I = I_{SC} - I_0 \left(e^{qV/nkT} - 1 \right) \quad (2.4)$$

where I_{SC} is the short-circuit current, I_o is the dark saturation current through the diode, k is the Boltzmann constant, T is the temperature and V is the applied voltage across the terminals, n is the ideality factor that measures of how closely the diode follows the ideal diode equation. A typical *I-V* characteristic curve is given in figure 2.10 by Luque [7]:

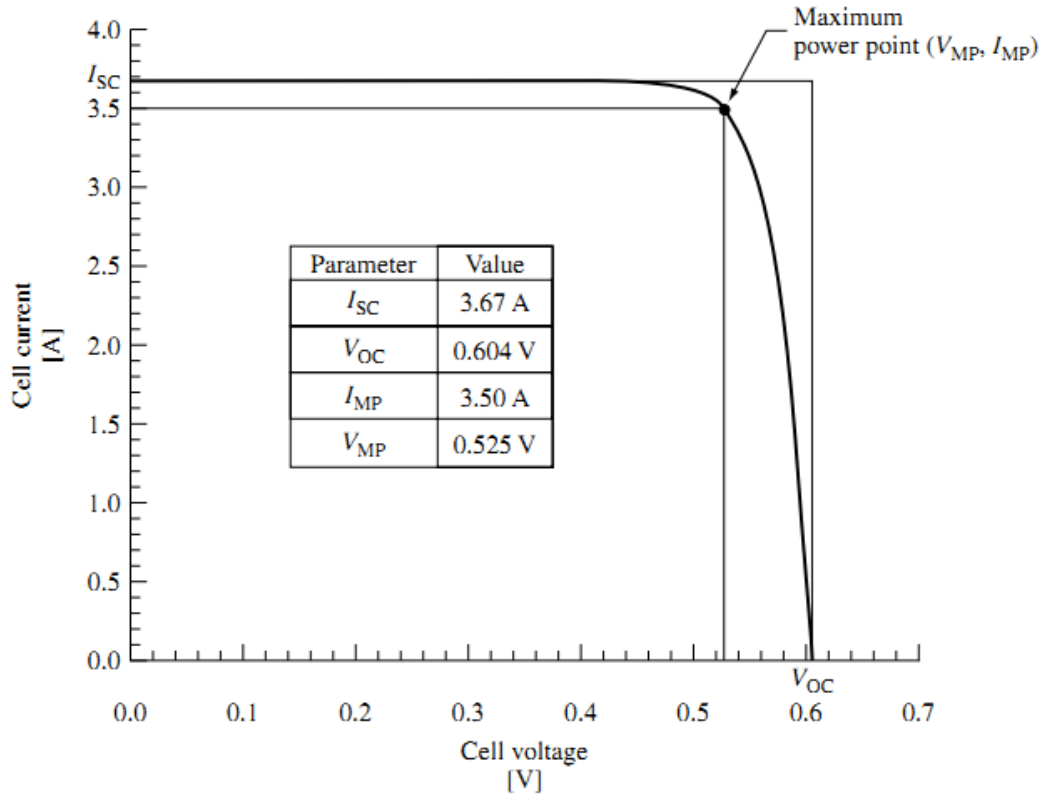| Parameter	Value
I_{SC}	3.67 A
V_{OC}	0.604 V
I_{MP}	3.50 A
V_{MP}	0.525 V

Figure 2.10: a typical *I-V* curve of a solar cell modeled according to the Schottky diode equation [7]. The numbers displayed in the table are not relevant in this project.

From this graph, several important parameters can be obtained to characterize the performance of a solar cell such as the open circuit voltage V_{OC}, short circuit current I_{SC}, maximum power ($I_{MP}V_{MP}$). A convenient parameter frequently used in solar cell calculation is the fill factor *FF*, which measures the *squareness* of the *I-V* curve:

$$FF = \frac{I_{MP}V_{MP}}{I_{SC}V_{OC}} \quad (2.5)$$

Finally, we define the power conversion efficiency of a solar cell as:

$$\eta = \frac{I_{MP}V_{MP}}{P_{incident}} = \frac{FFI_{SC}V_{OC}}{P_{incident}} \quad (2.6)$$

where $P_{incident}$ is the power of the incident light.

15

3 Experimental setups

The nanowires in this project were Ag@Cu$_2$O (silver core with cuprous oxide shell). Cuprous oxide is a p-type semiconductor, and can form a Schottky contact by using appropriate metal-semiconductor junction as described in section 2.2. Next, exploiting the rectifying property of a Schottky contact on the nanowire, a complete nanoscale solar cell device can be made according to the architecture described in figure 2.6. Therefore, the experiment in this project consists of two stages:

- Stage 1: Photolithography to deposit metal contacts on the Cu$_2$O shell and electrical characterization to verify Schottky behavior.
- Stage 2: Electron Beam Lithography to deposit contacts on the Cu$_2$O shell and Ag silver and electrical characterization to determine power conversion efficiency.

The fabrication technique used in this project was lithography, done at FOM Institute AMOLF. In general, the lithography process consists of writing patterns on a layer of photoresist using appropriate techniques (electron beam, UV, etc) followed by metal evaporation or other methods to deposit metal structures on the substrate. In this project, both photolithography and electron beam lithography were employed to deposit nanostructures on two ends of a nanowire, thereby establishing electrical contacts that can be used for appropriate characterizations. Specifically, photolithography was employed in stage 1 to establish the metal-semiconductor contacts and to verify the rectifying properties, while Electron Beam Lithography (EBL) was employed in stage 2 to fabricate a complete solar cell device and to analyze the photocurrent characteristics. Figure 3.1 and 3.2 present the schematic procedures of photolithography and electron beam lithography, respectively.

a: Coating first layer of lift-off resist (LOR) on the substrate

b: Coating second layer of photoresist (S1808)

c: Exposing sample under UV

d: Developing to remove the exposed area

e: Depositing metal film using thermal metal evaporation

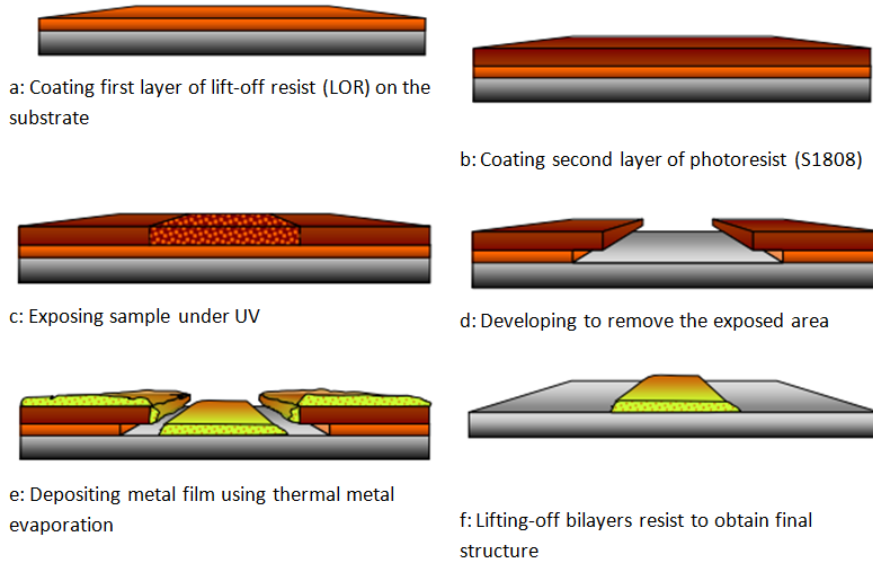f: Lifting-off bilayers resist to obtain final structure

Figure 3.1: Schematic procedures of UV lithography [15].

In 3.1a, the substrate is coated with a thin layer of lift-off resist. Next, in (b), a layer of photoresist is coated on the sample. The sample is exposed under UV light in (c). The exposed resist is removed in (d). In (e), metal is deposited on the sample using thermal evaporation. Finally, in (f), the remaining layers of photoresist to removed, lifting off the metal on top to obtain the desired pattern.
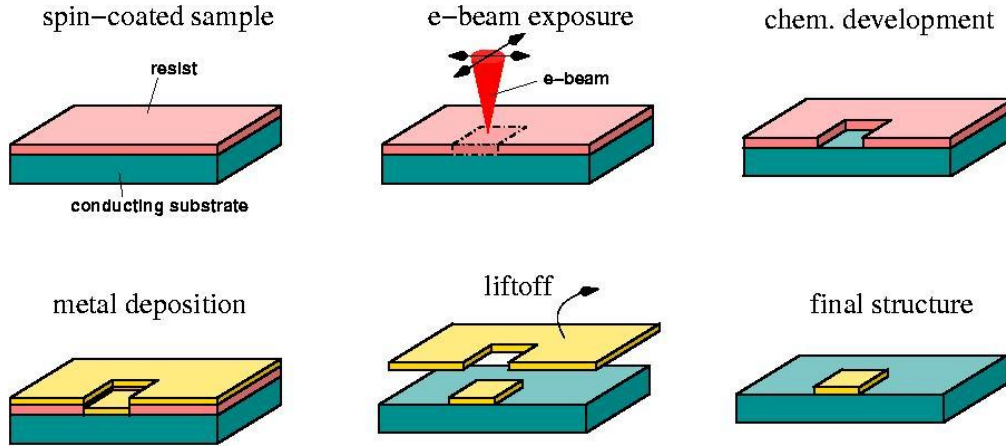

Figure 3.2: Schematic procedures of electron beam lithography [10]. A thin film of photoresist is deposited onto the substrate using spin-coating. The resist is then exposed with an electron beam to transfer the desired pattern. After exposure, chemical development removes the exposed pattern. Metal is then evaporated on top of the sample. "Liftoff" removes the material evaporated on top of the resist, leaving the final structure on the substrate.

## 3.1 Photolithography and Electrical Characterization

In stage one of this project, we employed photolithography to fabricate Aluminum-Cuprous Oxide metal-semiconductor contacts on the nanowires. We used two layers of different photoresists to create a slight undercut. This crucial additional step was added to facilitate the lift-off once the metal is evaporated onto the substrate. The nanowires were deposited randomly on the substrate using drop-casting. Next, polydimethylglutarimide Lift-off Resist A (LORA) was deposited using spincoating, followed by an additional layer of positive photoresist S1805. A photographic mask was placed on top of the sample, and the pattern was written on the sample by exposing the sample under UV light. Chemical development using tetramethylammonium hydroxide (MF319) removed the area that had been exposed under the UV light. Next, aluminum was deposited onto the sample using thermal evaporation. Finally, liftoff using acetone removed metal on the unexposed area. A schematic procedure of the fabrication process is given in figure 3.3. More details about the process can be found in Appendix B.
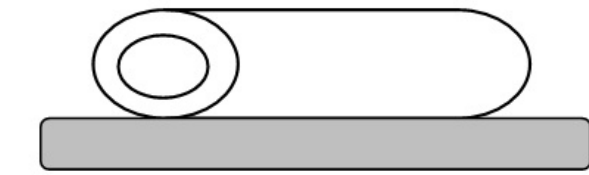
3.3a: Depositing a core-shell nanowire onto the substrate using drop casting.
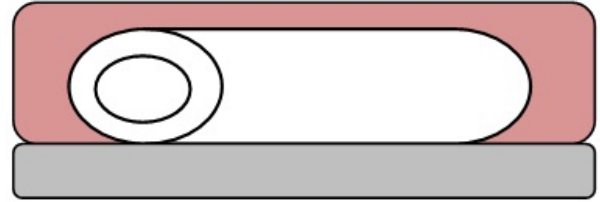
3.3b: Depositing lift-off resist A (LORA) using spin coating.
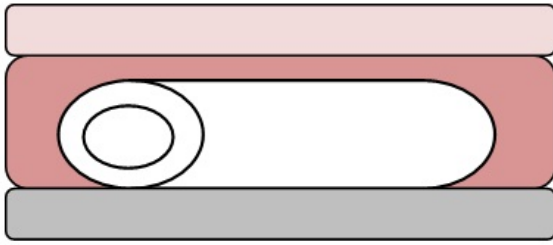
3.1c: Depositing S1805 photoresist using spin coating
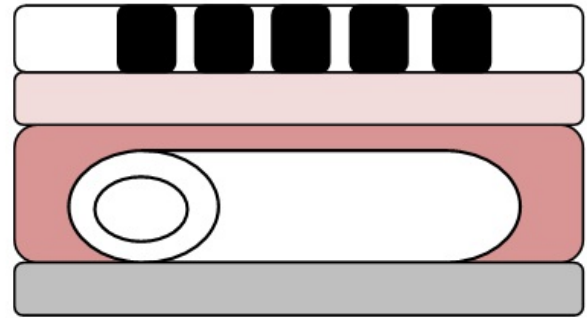
3.1d: Placing photographic mask on the sample.
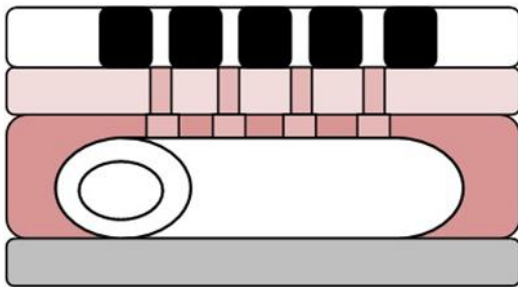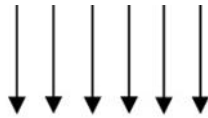
3.1e: Exposing the sample under UV light.
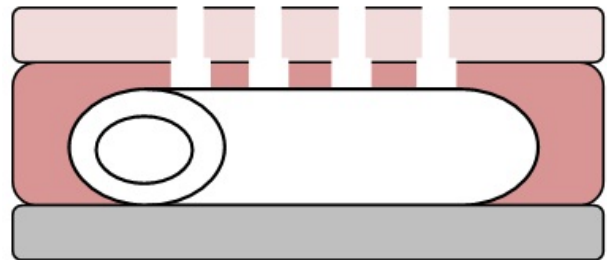
3.3f: Developing using MF319 to remove the exposed pattern.
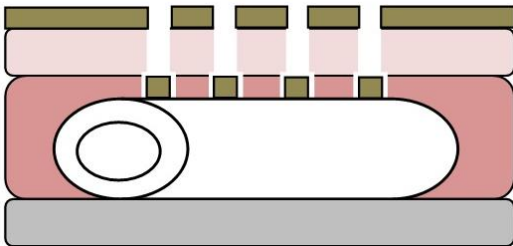
3.3g: Depositing Aluminum using thermal evaporation.
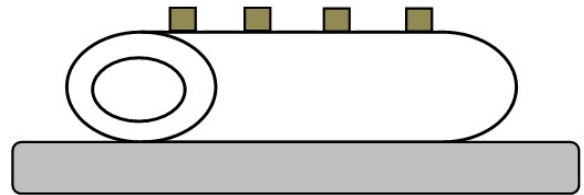
3.3h: Liftoff to remove the resists. A Schottky contact on the Cu_2O shell is established.

Figure 3.3: Schematic procedures of bilayer photolithography.

3.2 Electron Beam Lithography and Device Fabrication

In stage two of this project, in order to deposit the Schottky (rectifying) contact on the shell and Ohmic (non-rectifying) contact on the core, a multi-step EBL process was employed. The nanowires were deposited randomly on the substrate using drop-casting. Next, poly(methyl methacrylate) (PMMA) was deposited using spincoating, and a pattern was written (at one end of the nanowires) on the PMMA using an electron beam. Chemical development using Methyl Isobutyl Ketone (MIBK) removed the area that had been exposed under the electron beam. Next, aluminum was deposited onto the sample using thermal evaporation. Next, liftoff using acetone removed metal on the unexposed area. Again, PMMA was deposited using spincoating, followed by electron beam exposure (at the remaining end of the nanowires) and development using MIBK. The sample was then immersed in HCl to remove the Cu_2O shell, and silver was deposited using thermal evaporation. Liftoff removed unwanted metal. A schematic procedure of the fabrication process is given in figure 3.4.


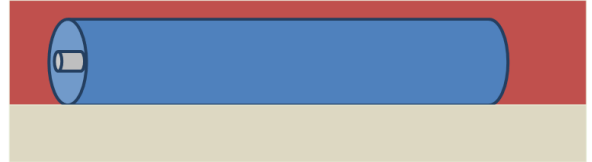3.4a: Depositing a core-shell nanowire onto the substrate using drop casting.

3.4b: Depositing PMMA photoresist using spin coating.
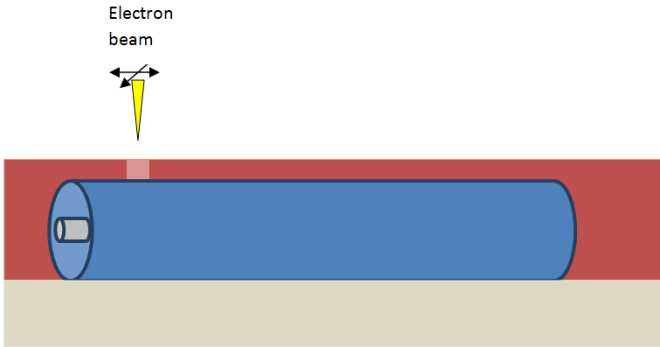
3.4c: Writing pattern using electron beam.

3.4d: Developing using MIBK to remove the pattern.

3.4e: Depositing Aluminum using thermal evaporation.

3.4f: Liftoff to remove the PMMA. A Schottky contact on the Cu_2O shell is established.
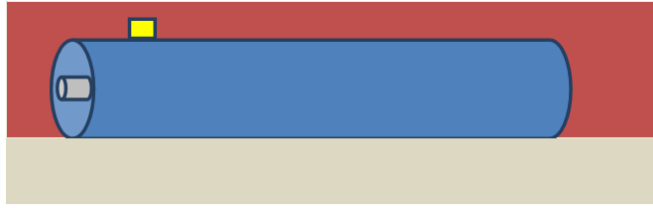
3.2g: PMMA photoresist deposition using spin coating.
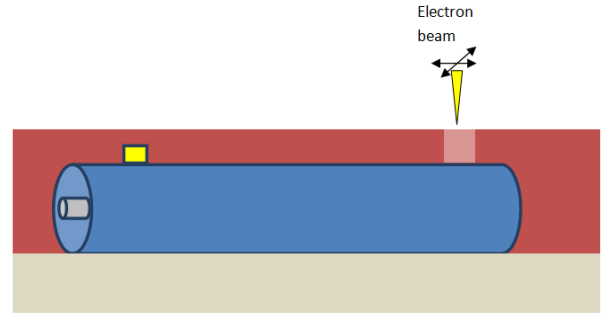
3.2h: Writing pattern using electron beam.
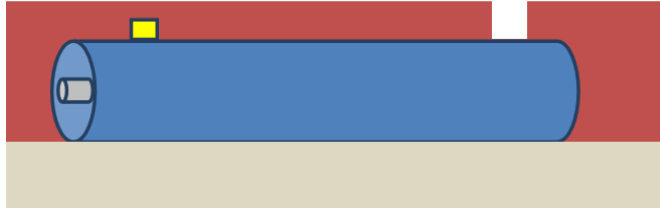
3.4i: Developing using MIBK to remove the pattern.

3.4j: HCl acid immersion to etch the Cu_2O shell, exposing the silver core.
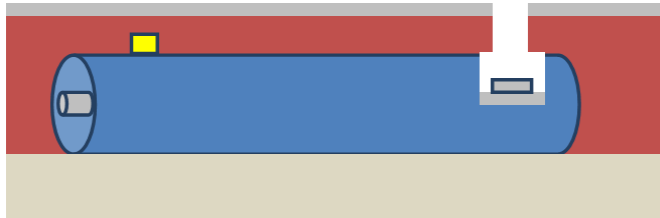
3.4k: Depositing silver using thermal evaporation.

3.4l: Liftoff to remove the PMMA. A metal contact on the silver core is established.

Figure 3.4: A schematic procedure of the multi-step EBL to establish Schottky contact on the core and a metal contact on the shell. We remind the reader that the Ohmic contact is between the core and the shell.

4   Results and Discussion

4.1   Electrical characterization

Using photolithography, we were able to deposit metal contacts on the shell of the nanowire. These contacts are connected to large measurement pads that can be probed by electrodes (Figure 4.1). Using micromanipulators tips, electrical measurements were performed on the nanowires to obtain the current-voltage characteristic graph (Figure 4.2a). The graph is anti-symmetrical. Measurements on different nanowires showed consistent overall trend of the graph.
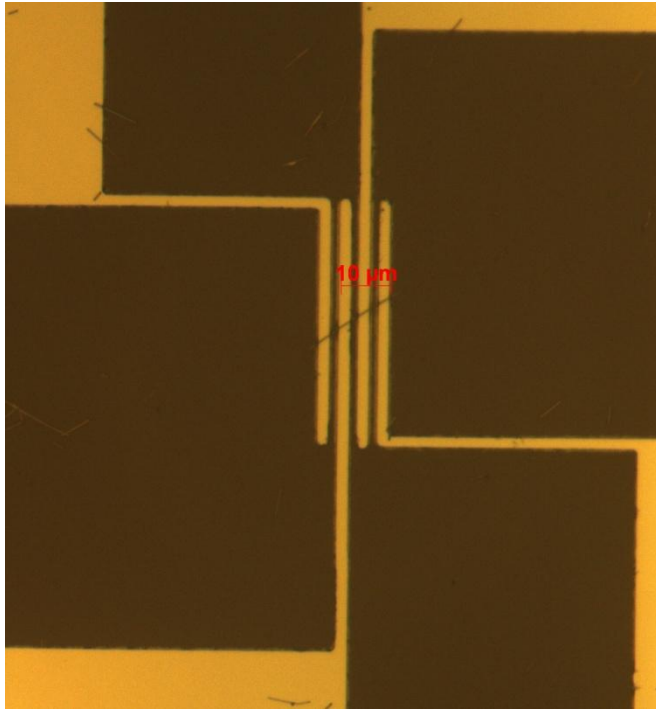
Figure 4.1: The nanowire sitting underneath and across the four aluminum fingers that are connected to large measurement pads.
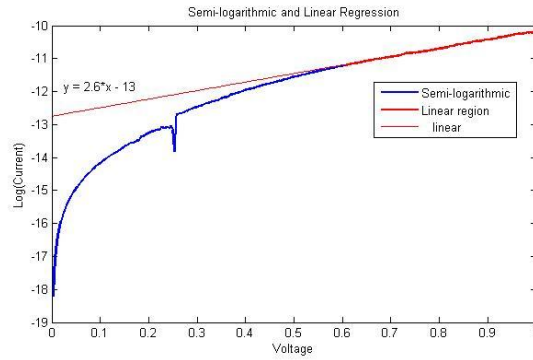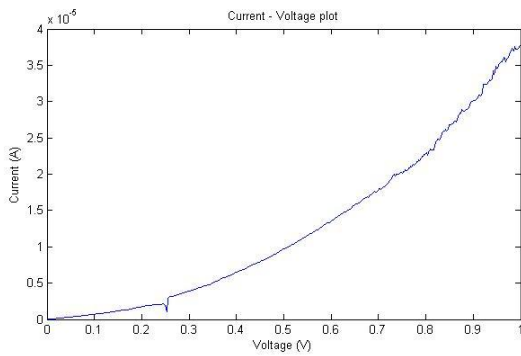
Figure 4.2a (left): Current-Voltage plot of the Schottky contact. Figure 4.2b (right): log(Current) – Voltage plot of the Schottky contact

In the absence of photocurrent, and taking into account the appropriate sign of the current's direction, the Schottky diode equation 2.4 in Section 2.3 can be rewritten as:

$$I = I_o \exp\left(\frac{qV}{nkT}\right)\left[1 - \exp\left(\frac{-qV}{nkT}\right)\right] \quad (4.1)$$

In the regime where $qV \gg nkT$ we then have:

$$I = I_o \exp\left(\frac{qV}{nkT}\right) \quad (4.2)$$

Taking the natural logarithm of both sides:

$$ln(I) = ln(I_0) + \frac{q}{nkT}V \quad (4.3)$$

Thus, by performing a fit on the linear part (large V) of the semi-logarithmic plot (Figure 4.2b), we can extract the saturation current and the ideality factor. From the linear fit, the saturation current and the ideality factor were determined to be 2.2µA and 15, respectively. In general, the saturation current in the dark can be seen as the current resulting from the recombination that is not doing any useful work. In a solar cell device, the saturation current should be as small as possible to increase the efficiency of the solar cell. The ideality factor measures how closely the device follows the ideal diode equation, and is equal to one in the ideal case. Since the derivation of the diode equation 2.4 involves several assumptions, high ideality factor may reveal useful information about secondary effects, and is a valuable method to predict the type of charge recombination in the device.

Having obtained the saturation current, the zero bias barrier height can be determined from the well-known equation [20]:

$$I_o = AA^*T^2 e^{\frac{-q\phi_b}{kT}} \quad (4.4)$$

where A is the effective diode area, A^* is the effective Richardson constant, T^2 is the temperature, q is the elementary charge, k is the Boltzmann constant, ϕ_b is the zero-bias barrier height. Assuming that the value of the effective Richardson constant (A^*) for Cu_2O at room temperature (303K) to be 100 Acm^{-2}K^{-2} [21], the effective diode area (A) to be 3*10^{-13} m^{-2} (the area at which Al and Cu_2O are in contact), the zero-bias barrier height was determined to be 0.24 eV.

The work function of Aluminum is $q\Phi_{Al} = 4.08 \ eV$ and the work function of cuprous oxide is $q\Phi_{Cu_2O} = 5.3 \ eV$. According to the band diagram, the Schottky potential barrier is $q(\Phi_{Cu_2O} - \Phi_{Al}) = 1.22 \ eV$. However, the value for potential barrier for the Schottky contact obtained from the data is 0.24 eV, which is significantly lower than the theoretically predicted value. According to Perraud [13], the high reverse current suggests a high density of localized

electronic states within the bandgap, which act as centers for generation-recombination. The effect of high concentration of surface states lead to Fermi level pinning phenomena, a situation where the band bending is essentially independent of the metal, regardless of the work function of the metal. As a suggestion for future research, different metals for Schottky contact should be used to verify the phenomena. In addition, even though Fermi level pinning limits the photovoltage of the solar cell device to a fixed value, it also allows more flexibility in designing the cell that meet other requirements (stability, material costs, etc)

4.2   Device Fabrication and Characterization

Using EBL, we were able to fabricate a complete solar cell device with Schottky contact on the cuprous oxide shell and Ohmic contact on the silver core. These contacts were connected to large measurement pads that can be probed by electrodes. A top-down image of a nanowire solar cell device viewed under the Scanning Transmission Electron Microscope is shown in figure 4.3.
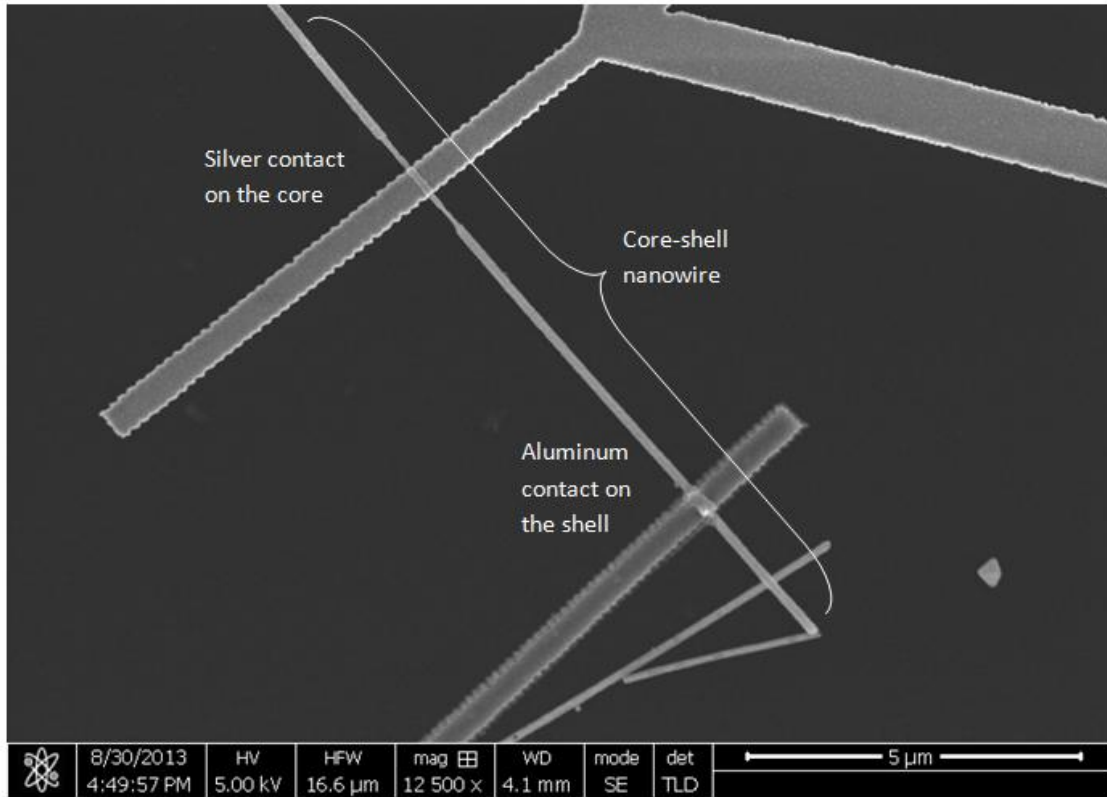
Figure 4.3: Top-down image of a nanowire solar cell device viewed under the Scanning Transmission Electron Microscope (STEM). The aluminum contact on the cuprous oxide shell is Schottky, and the core-shell contact is Ohmic. These contacts are connected to large measurement pads not shown in the image.

Electrical measurements were performed on the nanowires to obtain the current-voltage characteristic graph. However, the results are not consistent and hence no sensible information could be inferred at the writing point of this thesis. In addition, the multi-step EBL process is complicated with 12 intermediate steps, and we have yet maximized the efficiency of samples preparation. In general, out of the nine samples we initially prepared with drop-casting (step *a* in Figure 3.4), only two or three survived to the final stage (step *l* in Figure 3.4) for electrical characterization. In addition, the Al-Cu_2O interface was found to be irregular. Uncontrolled high temperature thermal deposition of aluminum and the mismatch between thermal expansion coefficients of aluminum and cuprous oxide may create voids and grains at the boundary. These structural defects can result in high leakage currents and low device performance. As such, we suggest further studies on the surface properties at the Al-Cu_2O interface.

5 Summary and Conclusions

The purpose of this thesis is to investigate the possibility of using nanowire as a building block for a new generation of solar cell.

In the theoretical part of this thesis, the interaction between the nanowire and light was described and reviewed under Mie Theory formalism. It was demonstrated that a semiconducting nanowire had high weighted absorption efficiency across the solar spectrum, and this high weighted absorption efficiency could be increased further by wrapping a thin layer of semiconducting material around the nanowire. Besides the enhanced weighted photon absorption, the core-shell nanowire also requires less semiconducting material as compared to conventional solid nanowire, which can potentially reduce the material cost. Next, Band Theory described how we can make use of the rectifying properties of metal-semiconductor junction to separate electron and hole in the semiconductor shell, providing the operating principle behind the core-shell nanowire solar cell device.

The experimental part of this thesis involved lithography processes to fabricate nanostructure to characterize the nanowire. In the first stage of the experiment, we used photolithography to build aluminum contacts on the shell of the wire to verify the rectifying properties of Al-Cu_2O metal-semiconductor junction. The ideality factor, the saturation current and the zero-bias were determined to be 15, 2.2μA and 0.24 eV, respectively. The high ideality factor indicated anomalous behaviors with regards to surface states and charge recombination that we have yet understood. In the second stage, using Electron Beam Lithography (EBL), we were able to fabricate a complete nanoscale solar cell device. However, the EBL process was not yet optimized with low throughput and inconsistent results. As a result, we were unable to determine the power conversion efficiency of the solar cell device. We suggested several directions for future research, namely the studies of surface properties to understand the charge recombination anomaly, and the optimization of the EBL process to determine the device's efficiency and consistency.

Two important successes of this thesis include the verification of Schottky behavior of the Al-Cu_2O metal-semiconductor junction, as well as the demonstration of the feasibility to fabricate a complete nanoscale solar cell device at the research laboratory level. As first, the low throughput in device production seemed to be problematic. However, it should be noted that there were constraints associated with laboratory research such as machine breakdowns, conflicts in timing among machine users, possible samples degradation while transferring them between labs, etc. Such problem can be easily eliminated in scalable fabrication processes at industrial level. More important questions that need to be addressed include the device's power conversion efficiency, stability under field operation, and mass production cost. Without these being answered, the core-shell nanowire is still far from being a replacement of today's Silicon-based solar cell technology.

References

[1] L.A. Haverkate, L.F. Feiner. Optical Properties of cylindrical nanowires. **2006**

[2] S.A. Mann, E. C. Garnett Extreme Light Absorption in Thin Semiconductor Films Wrapped around Metal Nanowires. *Nano Letters*, **2013**

[3] M. Wright, A. Uddin. Organic-inorganic Hybrid solar cells: A comparative review. *Solar Energy Materials & Solar Cells*. **2012**

[4] Y. Zhan, J. Zhao, C. Zhou, M. Alemayehu, Y. Li, Y.li. Enhanced photo absorption of single nanowire a-Si solar cells modulated by silver core. *Optical Express*, **2012**.

[5] G. Grzela. Mie Theory of Light Scattering by an infinite circular cylinder. Chapter 2: Theory of light scattering, absorption and waveguiding by individual nanowires. PhD Thesis, Eindhoven University of Technology **2013.**

[6] R.E. Hamam, A. Karalis, J.D. Joannopoulos, M.Soljacic Coupled-mode theory for general free-space resonant scattering of waves. *Physical Review,* **2007.**

[7] A. Luque, S. Hegedus. Solar Cell I-V Characteristics, *Handbook of Photovoltaic Science and Engineering*, **2003**

[8] Wikipedia: The Free Encyclopedia. Shockley–Queisser limit. Web: http://en.wikipedia.org/wiki/Shockley%E2%80%93Queisser_limit **2013**.

[9] National Center for Photovoltaics. Best Research-Cell Efficiency. Web: http://www.nrel.gov/ncpv/images/efficiency_chart.jpg **2013.**

[10] J.R. Krenn. Electron Beam Lithography. *Optical Nanotechnology/Nano-Optics*. Institute of Physics - Karl Franzens University Graz. Web: http://nanooptics.uni-graz.at/ol/work/m_ebl.html **2013.**

[11] S. Perraud, S. Poncet, S. Noel, M. Levis, P. Faucherand, E. Rouviere, P. Thony, C. Jaussaud, R. Delsol. Full process for integrating silicon nanowire arrays into solar cells. *Solar Energy Materials & Solar Cells*. **2009.**

[12] L. Tsakalakos, J. Balch, J. Fronheiser, B. Korevaar, O. Sulima, J. Rand. Fabricating nanowire-based solar cells on low-cost metal substrate. *Newsroom, SPIE- the international society for optics and photonics*. **2008.**

[13] J. Tang, Z. Huo, S. Brittman, H. Gao, P. Yang. Solution –processed for core-shell nanowires for efficient photovoltaic cells. *Letters, nature nanotechnology*. **2011.**

[14] The Brewer Science Blog. Overcoming spin-coating challenges for square substrates. *The Brewer Science Blog.* Web*:* http://info.brewerscience.com/Blog/bid/79975/Overcoming-spin-coating-challenges-for-square-substrates **2013.**

[15] LOR and PMGI Resists. *Micro Chem data sheet.* Web: http://microchem.com/pdf/PMGI-Resists-data-sheetV-rhcedit-102206.pdf **2013.**

[16] Microposit S1800 G2 Series Photoresists. *Electronic Materials.* Web: http://www.microresist.de/products/room_haas/pdf/microposit_s1800_g2_serie.pdf **2013.**

[17] Amsterdam Nanocenter. *Equipment Info.* Web: http://www.amsterdamnanocenter.nl/amsterdamnanocenter/equipment-info **2013.**

[18] General Experiment Techniques: Chapter 3. Web. **2014** http://www.study-on-line.co.uk/whoami/thesis/chap3.html

[19] E.H. Rhderick. Metal- Semiconductor contacts, Claredon, Oxford

[20] S. K. Cheung, N. W. Cheung. Extraction of Schottky diode parameters from forward current-voltage characteristics. *Applied Physics Letters*. 49, 85. **1986**

[21] E. S. Ikata, S.K. Adjepong. Electrical characteristics of Cu-Cu2O diodes fabricated by anodic oxidation. *Journal of Physics, D: Applied Physics*, 21. 1516-1518. **1988**

Appendix A: Maxwell equations and Mie's formal solutions [1]

Starting from Maxwell's equations with a periodic charge-free electromagnetic wave (time-dependent part $e^{-i\omega t}$), we have:

$$\nabla \times \vec{E} = i\omega\mu\vec{H}$$

$$\nabla \times \vec{H} = -i\omega\mu\vec{E}$$

Taking the curl of the two equations:

$$\nabla \times \left(\nabla \times \vec{E}\right) = i\omega\mu\left(\nabla \times \vec{H}\right) = \omega^2\epsilon\mu\vec{E}$$

$$\nabla \times \left(\nabla \times \vec{H}\right) = -i\omega\mu\left(\nabla \times \vec{E}\right) = \omega^2\epsilon\mu\vec{H}$$

It should be noted that the permittivity ϵ and permeability μ depend on the surrounding medium. By applying the vector identity, we have:

$$\nabla \times \left(\nabla \times \vec{A}\right) = \nabla\left(\nabla \bullet \vec{A}\right) - \nabla \bullet \left(\nabla\vec{A}\right)$$

We obtain the following (vector) differential equations:

$$\nabla^2\vec{E} + \omega^2\epsilon\mu\vec{E} = 0$$

$$\nabla^2\vec{H} + \omega^2\epsilon\mu\vec{H} = 0$$

In case of the sharp boundary between the nanowire and the surrounding medium, appropriate boundary conditions must be specified in order to solve analytically the differential equations above. There are 4 conditions that specify the tangential and normal components of the fields at the interface:

$$n \times \left(\vec{H}_2 - \vec{H}_1\right) = 0$$

$$n \times \left(\vec{E}_2 - \vec{E}_1\right) = 0$$

$$n \cdot \left(m_2^2\vec{H}_2 - m_1^2\vec{H}_1\right) = 0$$

$$n \cdot \left(\vec{E}_2 - \vec{E}_1\right) = 0$$

where m is the (complex) refractive index of the medium at the frequency $\omega=kc=2\pi\lambda$ of the wave and n is the normal vector to the surface.

We are now ready to solve the boundary value problem of the wave equation. In general, the procedure to solve the vector Maxwell wave equations consists of the following steps:

- Solving for the *scalar* wave equation ψ
- Solving for the *vector* wave equation $\vec{M}_\psi, \vec{N}_\psi$ that depend on ψ
- Obtaining $\vec{E}$ and $\vec{H}$ by taking the appropriate linear combinations of $\vec{M}_\psi$ and $\vec{N}_\psi$

Assume an infinitely long cylinder ($L \gg 2R$). In the case of cylindrical coordinates, the rectangular part automatically satisfies the (scalar) wave equation:

$$\Delta \psi + k_0^2 m^2 \psi = 0$$

If we define $\vec{M}_\psi$ and $\vec{N}_\psi$ as:

$$\vec{M}_\psi = \nabla \times (\psi \cdot \hat{e}_z)$$

$$\vec{N}_\psi = \frac{1}{mk_0} \nabla \times (\vec{M}_\psi)$$

Then both $\vec{M}_\psi$ and $\vec{N}_\psi$ satisfy the vector field wave equations, and the solutions to Maxwell's equations are:

$$\vec{E} = \vec{M}_v + i\vec{N}_u$$

$$\vec{H} = m\vec{M}_u - im\vec{N}_v$$

where u and v are the two independent solutions of the scalar wave equation ψ.

In order to solve for ψ in the scalar wave equation, we use separation of variables in cylindrical coordinates.

$$\left(\frac{\partial^2}{\partial \rho^2} + \frac{1}{\rho}\frac{\partial}{\partial \rho} + \frac{1}{\rho^2}\frac{\partial^2}{\partial \phi^2} + \frac{\partial^2}{\partial z^2} + k_0^2 m^2 \right)\psi = 0 \rightarrow Ansatz\ \varphi_n = P(\rho)\Phi(\phi)Z(z)$$

to obtain a solution (together with the time-dependent part):

$$\varphi_n = P(\rho)\Phi(\phi)Z(z)T(t) = B_n\left(\rho\sqrt{k_0^2 m^2 - g^2}\right)e^{in\phi}\, e^{igz}\, e^{-i\omega t}$$

where B_n is any Bessel function of order n that comes from the differential equation of the ρ coordinate, g is arbitrary. The solution ψ is of course an appropriate linear combination of φ_n. We then obtain $\vec{M}_\psi$ and $\vec{N}_\psi$:

$$\vec{M}_{\varphi_n} = \begin{pmatrix} \dfrac{in}{\rho} \\[2mm] -\dfrac{\partial}{\partial\rho} \\[2mm] 0 \end{pmatrix} \varphi_n \; and \, \vec{N}_{\varphi_n} = \frac{1}{mk_0} \begin{pmatrix} ig\dfrac{\partial}{\partial\rho} \\[2mm] -\dfrac{ng}{\rho} \\[2mm] m^2 k_0^2 - g^2 \end{pmatrix} \varphi_n$$

And finally the electrical and magnetic fields in terms of cylindrical coordinates (ρ, ϕ, z) can be obtained:

$$\vec{E}(\rho, \phi, z) = \begin{pmatrix} \displaystyle\sum_{n=-\infty}^{\infty} \dfrac{in}{\rho} v_n - \dfrac{g}{mk_0}\dfrac{\partial u_n}{\partial\rho} \\[4mm] \displaystyle\sum_{n=-\infty}^{\infty} -\dfrac{\partial v_n}{\partial\rho} - \dfrac{ing}{mk_0\rho} u_n \\[4mm] \displaystyle\sum_{n=-\infty}^{\infty} \dfrac{i(m^2 k_0^2 - g^2)}{mk_0} u_n \end{pmatrix} \; and \; \vec{H}(\rho, \phi, z) = \begin{pmatrix} \displaystyle\sum_{n=-\infty}^{\infty} \dfrac{inm}{\rho} u_n + \dfrac{g}{k_0}\dfrac{\partial v_n}{\partial\rho} \\[4mm] \displaystyle\sum_{n=-\infty}^{\infty} -m\dfrac{\partial u_n}{\partial\rho} - \dfrac{ing}{k_0\rho} v_n \\[4mm] \displaystyle\sum_{n=-\infty}^{\infty} -\dfrac{i(m^2 k_0^2 - g^2)}{k_0} v_n \end{pmatrix}$$

Solution to scattering problem using Mie solution

After the infinite series solutions to the wave equations have been established, the scattering problem can be studied. For simplicity, we assume a polarized incoming wave incident at an angle θ to the cylinder's normal axis.
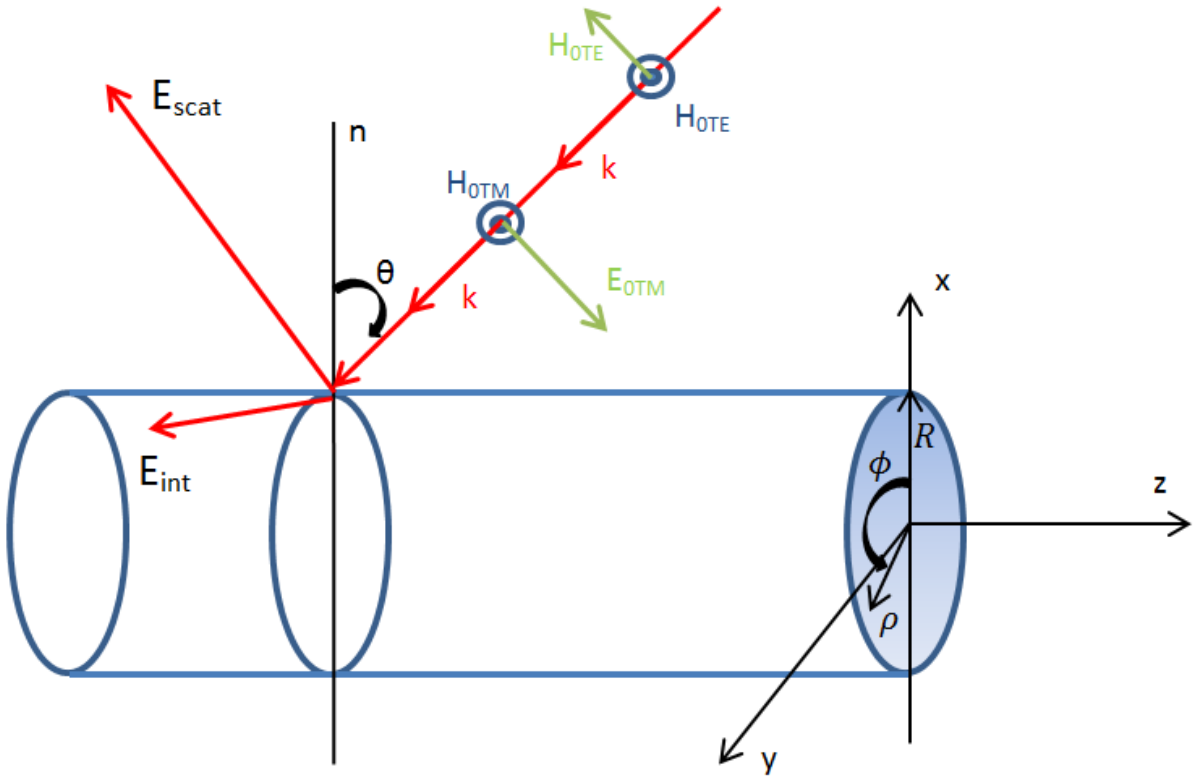
Figure A.1: Coordinates for the scattering problem. The incoming wave with the incident angle θ is shown with the electric and magnetic fields in two different modes TE and TM. Figure adapted from [1].

The incoming wave is represented by the following function:

$$\psi_0 = \tilde{E}_0 e^{-i(hz+\omega t)} \sum_{n=-\infty}^{\infty} (-i)^n J_n(l\rho) e^{in\phi}$$

where $h \equiv k_0 \sin\theta$, $l \equiv k_0 \cos\theta$ and $J_n(x)$ is the integral order Bessel function.

The polarized incoming wave is resolved into two components (or modes):

- Transverse Magnetic Mode (TM mode): the magnetic field of the incident wave is normal to the cylinder axis. This can be done by setting $u_n = \frac{1}{il}\tilde{E}_0(-i)^n \varphi_n$ (with $g = -h$, $B_n = J_n$) and $v_n = 0$.
- Transverse Electric Mode (TE mode): the electric field of the incident wave is normal to the cylinder axis. This can be done by setting $v_n = \frac{1}{il}\tilde{E}_0(-i)^n \varphi_n$ and $u_n = 0$

Interestingly, unlike the incident wave, the solutions for the scattered and internal (absorbed) scalar waves consist of TM or TE, together with an additional "cross mode". The signature of the internal fields is pure TM or TE only for a cylinder illuminated perpendicularly to its axis ($\theta=0$). The general expression for the fields inside and outside is given by [1]

TM mode:

- $\rho > R$:
$$u_{n\,TM} = \tilde{E}_0 F_n \left[J_n(l\rho) - b_{n\,TM} H_n^{(1)}(l\rho) \right]$$
$$v_{n\,TM} = \tilde{E}_0 F_n \left[a_{n\,TM} H_n^{(1)}(l\rho) \right]$$

- $\rho < R$:
$$u_{n\,TM} = \tilde{E}_0 F_n \left[d_{n\,TM} J_n^{(1)} \left(\sqrt{m^2 k_0^2 - h^2}\, \rho \right) \right]$$
$$v_{n\,TM} = \tilde{E}_0 F_n \left[c_{n\,TM} J_n^{(1)} \left(\sqrt{m^2 k_0^2 - h^2}\, \rho \right) \right]$$

TE mode

- $\rho > R$
$$u_{n\,TE} = \tilde{E}_0 F_n \left[b_{n\,TE} H_n^{(1)}(l\rho) \right]$$
$$v_{n\,TE} = \tilde{E}_0 F_n \left[J_n(l\rho) - a_{n\,TE} H_n^{(1)}(l\rho) \right]$$

- $\rho < R$

$$u_{n\,TE} = \tilde{E}_0 F_n \left[d_{n\,TE} J_n^{(1)} \left(\sqrt{m^2 k_0^2 - h^2} \rho \right) \right]$$

$$v_{n\,TE} = \tilde{E}_0 F_n \left[c_{n\,TE} J_n^{(1)} \left(\sqrt{m^2 k_0^2 - h^2} \rho \right) \right]$$

where $F_n \equiv \frac{1}{il} e^{-i(hz-\omega t)} (-i)^n e^{in\phi}$ and $J_n^{(1)}(x)$ and $H_n^{(1)}(x)$ and are the Bessel and Hankel functions of the first kind, respectively.

Substituting u_n and v_n into Mie's formal solutions obtained earlier in III.1.a

$$\vec{E}(\rho, \phi, z) = \begin{pmatrix} \displaystyle\sum_{n=-\infty}^{\infty} \frac{in}{\rho} v_n - \frac{g}{mk_0} \frac{\partial u_n}{\partial \rho} \\[2ex] \displaystyle\sum_{n=-\infty}^{\infty} -\frac{\partial v_n}{\partial \rho} - \frac{ing}{mk_0\rho} u_n \\[2ex] \displaystyle\sum_{n=-\infty}^{\infty} \frac{i(m^2 k_0^2 - g^2)}{mk_0} u_n \end{pmatrix} \quad \text{and} \quad \vec{H}(\rho, \phi, z) = \begin{pmatrix} \displaystyle\sum_{n=-\infty}^{\infty} \frac{inm}{\rho} u_n + \frac{g}{k_0} \frac{\partial v_n}{\partial \rho} \\[2ex] \displaystyle\sum_{n=-\infty}^{\infty} -m\frac{\partial u_n}{\partial \rho} - \frac{ing}{k_0\rho} v_n \\[2ex] \displaystyle\sum_{n=-\infty}^{\infty} -\frac{i(m^2 k_0^2 - g^2)}{k_0} v_n \end{pmatrix}$$

to obtain the fields inside and outside the cylinder with respect to the mode of the incoming wave as an infinite series of cylindrical vector harmonics. For example, the electric and magnetic fields of the scattered waves when the incident wave is in TM mode are:

$$\vec{E}_{scat\,TM} = \tilde{E}_0 \sum_{n=-\infty}^{\infty} F_n \left[a_{n\,TM} \begin{pmatrix} in/\rho \\ -\partial/\partial\rho \\ 0 \end{pmatrix} H_n^{(1)}(l\rho) - i b_{n\,TM} \begin{pmatrix} ih\frac{\partial}{\partial\rho}/mk_0 \\ nh/mk_0\rho \\ m^2 k_0^2 - h^2/mk_0 \end{pmatrix} H_n^{(1)}(l\rho) \right]$$

$$\vec{H}_{scat\,TM} = \tilde{E}_0 \sum_{n=-\infty}^{\infty} F_n \left[a_{n\,TM} \begin{pmatrix} -h\frac{\partial}{\partial\rho}/k_0 \\ inh/k_0\rho \\ -i(m^2 k_0^2 - h^2)/k_0 \end{pmatrix} H_n^{(1)}(l\rho) - i b_{n\,TM} \begin{pmatrix} inm/\rho \\ -m\frac{\partial}{\partial\rho}/k_0\rho \\ 0 \end{pmatrix} H_n^{(1)}(l\rho) \right]$$

The coefficients $a_{n\,TM}, b_{n\,TM}, c_{n\,TM}, d_{n\,TM}$ which appear in the scattering and internal fields are determined by the incident angle θ and the cylinder's radius R. Recall that the boundary conditions specified in III.1.a require the continuity of the tangential components of $\vec{E}$ and $\vec{H}$. Therefore, the tangential components of Mie's formal solutions (ϕ and z components) have to be continuous when $\rho = R$. As a consequence, we obtain four solvable algebraic equations. The solving process is computationally intensive, and we only mention the final results obtained from [1]:

$$a_{n\,TM}(R,\theta) = \frac{isin(\theta)n(m^2-1)(N_n^{-1}-N_n^{-1})}{lR\left[\left(\frac{j}{k_0}\right)^2 L_n - (m^2+1)\frac{j}{k_0}D_n + L_n^{-1}(C_n - m^2 D_n^2)\right]}$$

$$b_{n\,TM}(R,\theta) = \frac{H_n^{(1)'}(lR)\left[\left(\frac{j}{k_0}\right)^2 K_n - m^2\frac{j}{k_0}D_n\right] + H_n^{(1)'}(lR)\left[\frac{j}{k_0}D_n K_n + m^2 D_n^2 - C_n\right]}{H_n^{(1)}(lR)M_n\left[\left(\frac{j}{k_0}\right)^2 L_n - (m^2+1)\frac{j}{k_0}D_n + L_n^{-1}(C_n - m^2 D_n^2)\right]}$$

$$c_{n\,TM}(R,\theta) = \frac{l^2}{j^2}\left[\frac{a_{n\,TM}(R,\theta)H_n^{(1)}(lR)}{J_n(jR)}\right]$$

$$d_{n\,TM}(R,\theta) = \frac{ml^2}{j^2}\left[\frac{J_n(lR) - b_{n\,TM}(R,\theta)H_n^{(1)}(lR)}{J_n(jR)}\right]$$

$$a_{n\,TE}(R,\theta) = \frac{H_n^{(1)'}(lR)\left[\left(\frac{j}{k_0}\right)^2 K_n - \frac{j}{k_0}D_n\right] + H_n^{(1)'}(lR)\left[m^2\frac{j}{k_0}D_n K_n + m^2 D_n^2 - C_n\right]}{H_n^{(1)}(lR)M_n\left[\left(\frac{j}{k_0}\right)^2 L_n - (m^2+1)\frac{j}{k_0}D_n + L_n^{-1}(m^2 D_n^2 - C_n)\right]}$$

$$b_{n\,TE}(R,\theta) = -a_{n\,TM}(R,\theta)$$

$$c_{n\,TE}(R,\theta) = \frac{l^2}{j^2}\left[\frac{J_n(lR) - b_{n\,TE}(R,\theta)H_n^{(1)}(lR)}{J_n(jR)}\right]$$

$$d_{n\,TM}(R,\theta) = \frac{ml^2}{j^2}\left[\frac{a_{n\,TE}(R,\theta)H_n^{(1)}(lR)}{J_n(jR)}\right]$$

where:

$$j \equiv \sqrt{m^2 k_0^2 - h^2}, l \equiv k_0 cos\theta$$

$$C_n \equiv \frac{(m^2 - 1)^2 n^2 \tan^2 \theta}{j^2 R^2}$$

$$D_n \equiv \cos\theta \, \frac{J_n'(jR)}{J_n(jR)}$$

$$K_n \equiv \frac{J_n'(lR)}{J_n(lR)}, L_n \equiv \frac{H_n^{(1)'}(lR)}{H_n^{(1)}(lR)}$$

$$M_n \equiv \frac{H_n^{(1)'}(lR)}{J_n(lR)}, N_n \equiv \frac{H_n^{(1)}(lR)}{J_n(lR)}$$

$$O_n \equiv \frac{H_n^{(1)'}(lR)}{J_n'(lR)}$$

Appendix B: Photolithography process to test for Schottky-Ohmic contacts on the nanowires

1)   Overview: This appendix describes in detail the photolithography process to establish metal contacts at each end of a core-shell Ag@Cu$_2$O nanowire. Due to the complex nature of the contacting process, a series of sophisticated equipment had to be used, and all steps (except for sample preparation and material evaporation) were done in the cleanroom at FOM Institute AMOLF, which has comprehensive fabrication capabilities. A step-by-step overview of the process is shown below:

- Depositing nanowires on a silicon nitride-coated wafer by drop-casting
- Spin coating photoresist on the wafer
- Exposing the resist using a UV Lithography system (MJB3 machine)
- Developing and removal of the exposed photoresist
- Depositing metal using thermal metal evaporation
- Lift-off
- I-V Characterization

Instead of using the conventional single layer of photoresist, we applied two layers of different photoresists to create a slight undercut. This crucial additional step was added to facilitate the lift-off once the metal is evaporated onto the substrate.
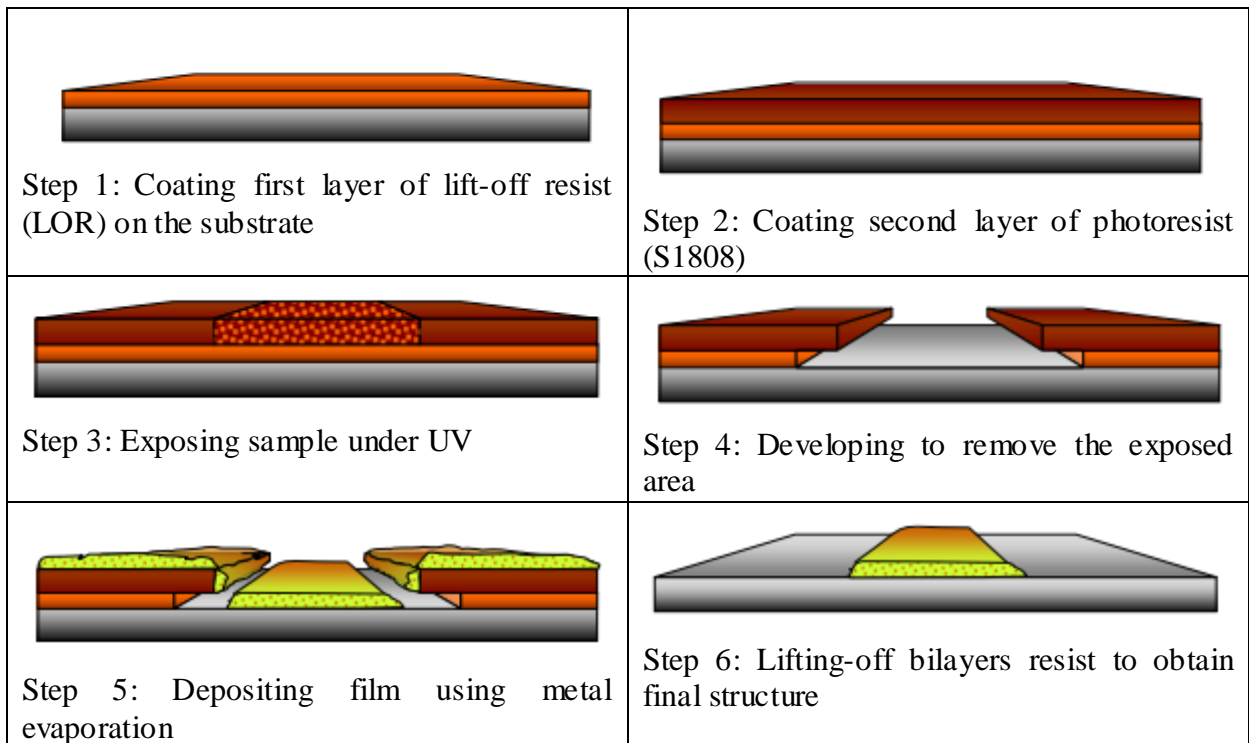

Step 1: Coating first layer of lift-off resist (LOR) on the substrate	Step 2: Coating second layer of photoresist (S1808)
Step 3: Exposing sample under UV	Step 4: Developing to remove the exposed area
Step 5: Depositing film using metal evaporation	Step 6: Lifting-off bilayers resist to obtain final structure

Figure B.1: Schematic procedures of bilayer photolithography [15].

2) Establishing metal contact

i. Sample preparation

The substrates used in this process were cleaved from 400μm silicon wafers, which are coated with a 50μm silicon nitride. It is imperative that the substrates must be cleaned to remove unwanted contaminants that may affect the lithography process. Residual particles on the wafer could lead to poor adhesion and affect the lift-off process (discussed in section III.2.v). Under normal circumstances, silicon wafers are cleaned using "Piranha Etching". However, for this thesis, it was found that if the wafers were only used for the UV-dose testing, it was sufficient to just sonicate the wafers in acetone for 15 minutes, followed by rinsing in acetone and then isopropyl alcohol (IPA).

To maximize throughput, nine 1x1 cm^{2}substrates were prepared prior to each experiment. Each substrate was dipped in a ethanol solution containing the nanowires for three to five minutes, depending on the nanowire concentration. Longer dip times were required after repeated uses of a nanowire solution to ensure necessary density of the nanowires on the silicon wafer. The samples then underwent a brief treatment with fresh ethanol for one minute to remove traces of organic solvents and then were blown completely dry before proceeding with the next step.

ii. Bilayer spincoating

The photoresists used in this process were LORA and S1805.

- LORA (Lift-off Resist A) is based on polydimethylglutarimide from Microchem[TM]. It has excellent adhesion properties and thus primers (such as HDMS) are not required. The undercut rate is tunable by the pre-baking time. It is recommended by the manufacturer that, for a clean lift-off processing, the LORA thickness should be typically 25% thicker than the deposited metal film (Microchem, 2013).
- S1805 is a positive photoresist from the series S18xx from Microposit[TM]. The resist used in this project was a dyed version to facilitate working with reflective silicon substrates.
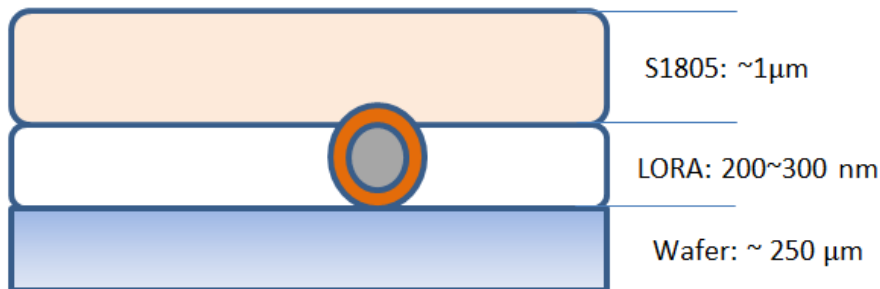

Figure B.2: Schematic cross-sectional view of bilayer thin films with a core-shell nanowire deposited on top of a silicon wafer. Image is not drawn accurately to scale.

The thickness of the film depends on the spin speed. For S1805, the required speed was obtained by extrapolating the spincurve provided by the manufacturer. For LORA, the required speed was obtained by interpolating the spincurve obtained at 3 different speeds.
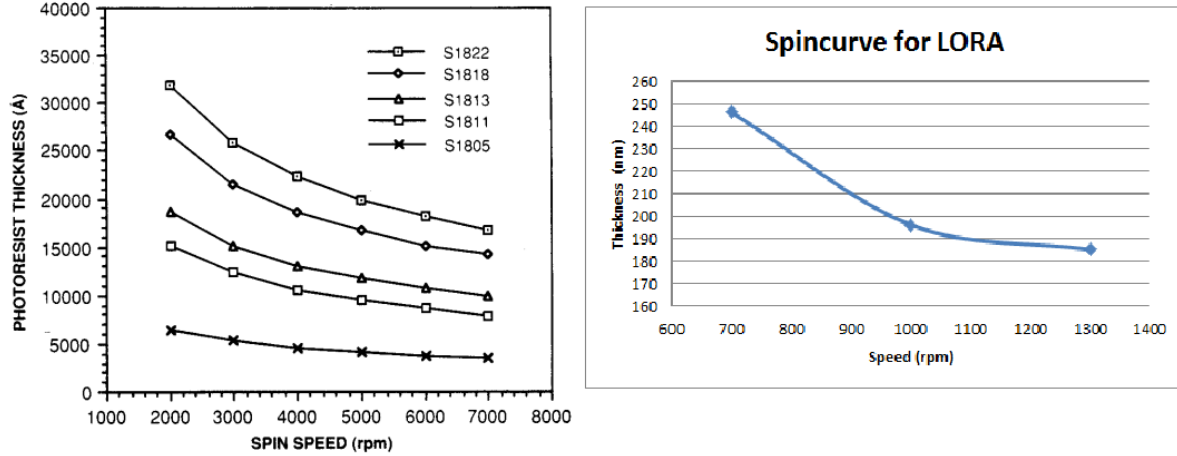

Figure B.3: Left: spincurve for S18xx families [16]. Right: spincurve for LORA obtained from measuring film thickness at spin speed of 700, 1000 and 1300 rpm.

Whenever possible, the resist was spincoated on the wafers as soon as the dropcasting process was completed to prevent possible degradation of the nanowires in ambient conditions. Before spinning, the wafers were pre-baked at 180°C for 3 minutes to remove traces of moisture. The pre-bake also promotes good adhesion of the LORA to the resist.

To start the spincoating, the wafer was first carefully centered on the chuck of the spincoater and held fixed by the machine's vacuum pump. LORA resist was then gently dropped onto the water using a syringe, avoiding creating bubbles as much as possible. The wafer was then spun at 1000rpm for 40 seconds with the acceleration of 1000rpm/s. It was then baked at 180°C for 3 minutes. The wafer was then transferred onto the chuck again. S1805 was next gently dropped onto the wafer in the same manner as the previous step. The wafer was spun at 1000rpm for 40 seconds with the acceleration of 1000rpm/s, following by baking at 115°C for 1 minute.

A recurring problem which occurred during the spincoating process was the edge effect. When a square substrate was spun, the corners created a turbulence that resulted in a poor coat quality near the edge. As a result, the resist built up at the edges with higher thickness than the central part. This non-uniformity severely affected the mask alignment process in the next step, because the UV lithography mask couldn't be brought in uniform contact to the resist, which lead to a decreased resolution during exposure. Usually higher spin speeds are used to prevent the build-up of resist at sample edges, but the requirements, posed by the necessary metal thickness and the lift-off procedure, limited the spin speeds to lower values. To resolve the problem, a cotton swab was dipped in lifting-off solution to carefully dissolve the resist built up at the edge.
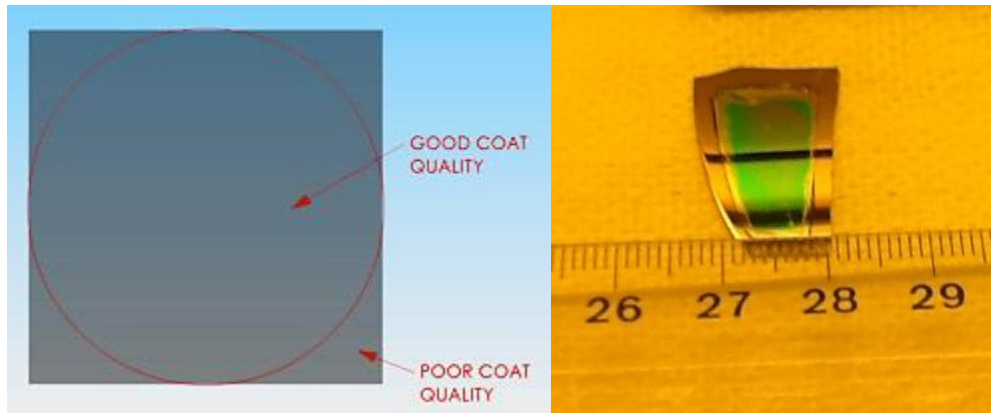
Figure B.4: Left: Edge effect from using a square wafer during spincoating [14]. Right: sample after removing photoresist at the edge. The scale is in centimeter

iii.   Photolithography

After the deposition of thin layers of photoresists on the wafer, the UV-lithography was carried out with the SUSS MicroTec MJB3 lithography system. The system consists of an UV light source, a stage with microcontrollers to position the sample, a mask holder to expose the desired pattern on the resist and an optical microscope with a CCD camera, which is connected to a monitor.

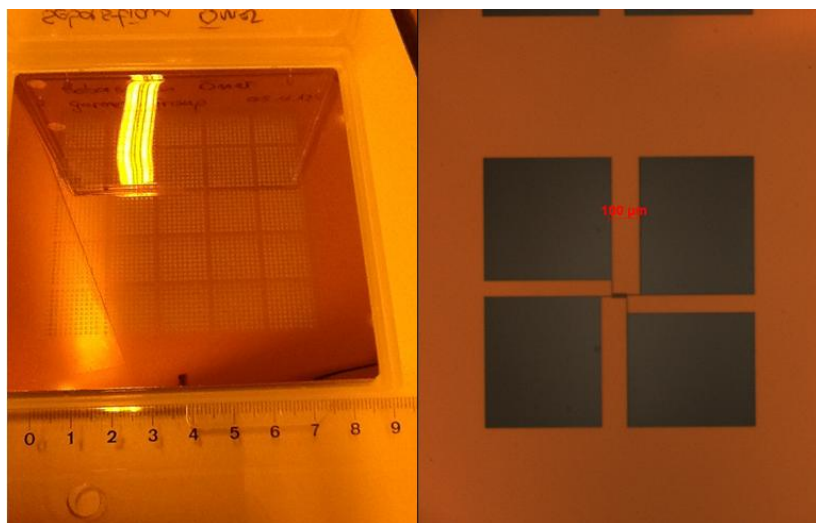Figure B.4: MJB3system with various components [17].

Figure B.5: Chromium mask used in this project. Left: An overview of the mask. The mask consists of 5x5 arrays, each array contains 10x10 fingers-pads patterns. The scale is in centimeters. Right: magnified view of a fingers-pads configuration. The 4 fingers (2 µm apart) are connected to large pads at the corners that can be contacted using micromanipulators tips for electrical measurements.

The samples were put on the stage and brought close to the mask. The resist-covered area was then aligned with the mask's windows using the micrometer stage controller. The stage was then raised up further until the wafer was in soft contact with the mask. The critical step of this setup is to ensure that the mask and the substrate are in even contact with no air gap between the mask and the wafer. This can be achieved by adjusting the stage height using the stage micro controller(labeled "Stage controller (z) in figure 3.4) and removing the edge build-up on the wafer (already done in the previous spincoating step). After good contact with the mask was ensured, the wafer was exposed under UV light. It was then developed in MF319 (Microposit^{TM}).

In all lithography techniques, the UV dose measurement is an important factor. There is a trade-off between exposure time and developing time. Longer exposure times ensure that the photoresist in the exposed area can be removed easily. Below this dose, the exposed area may not be fully removed during development. However, high doses also lead to a stronger undercut, which can potentially cut through the middle fingers and remove them altogether during the development process if the developing time is too long. A considerable amount of time had to be spent to fine-tune these two parameters to achieve the most uniform structure, besides taking care of a very good contact between the mask and the wafer. Based on previous experience, the exposure dose varies between 17 to 24 seconds and developing time varies between 45 to 75 seconds. It was found out, solely based on trials and errors, that a combination of 20 seconds exposure time and 70 seconds developing time would give the most satisfactory results, for a resist thickness of 1.2 µm.
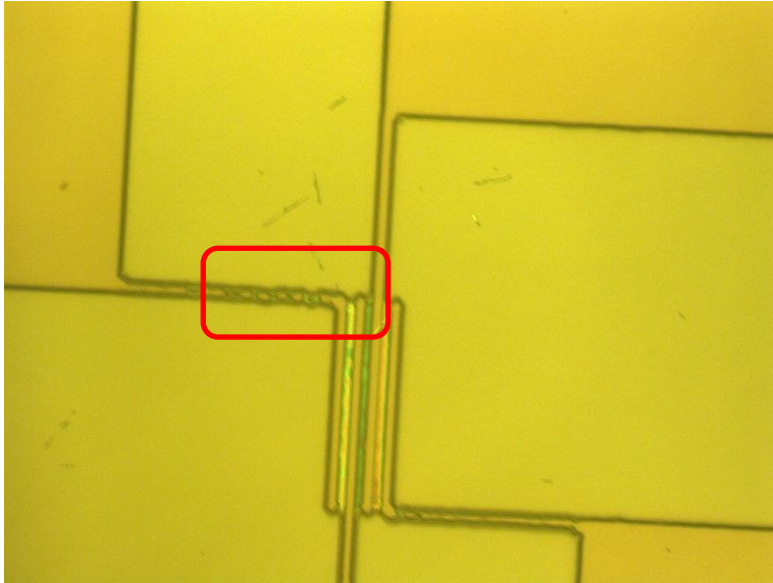
Figure B.6: Underexposed area that still shows trenches after developing, which will lead to broken contact fingers after metal evaporation and lift-off.
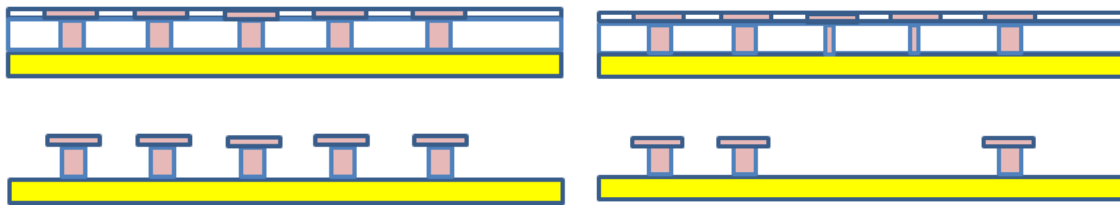

Figure B.7: Possible outcomes of the undercut using bilayer method. Left: Optimal case when the exposure and developing time is such that the undercut is not too strong. After metal deposition and lift-off, there will be 4 metal fingers between 5 columns. Right: Too long exposure and developing times remove the middle fingers altogether and only 2 metal fingers are left after developing.
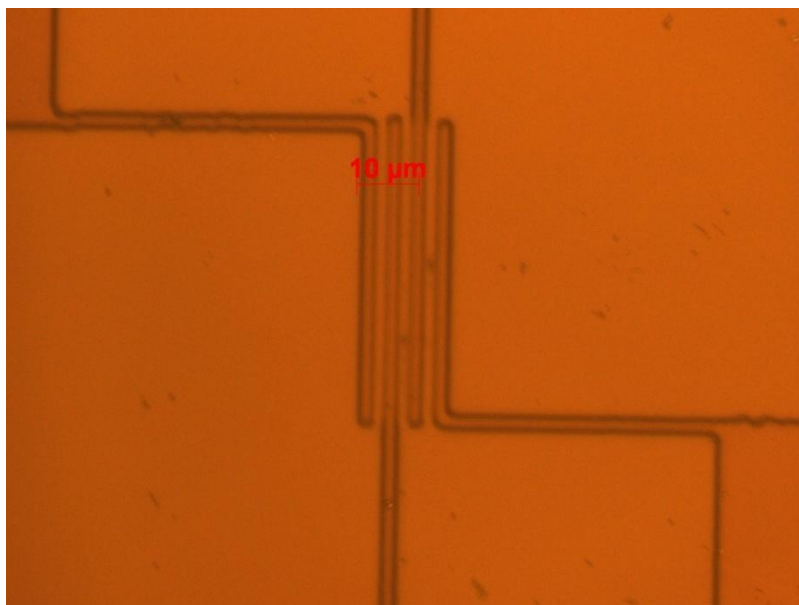
Figure B.8: Result for a dose test. After developing, the mask's pattern was successfully transferred to the substrate. Notice the slight undercut (double lines) because of the bilayer resist.

iv.   Metal deposition

The metal was deposited onto the water through thermal evaporation using a home-built device AMOLF. A controlled high current was used to heat up a tungsten boat that contained the source material, heating it up to the material's evaporation temperature. The vacuum allowed vapor particles to travel directly to the target substrate and then condensed back to a solid state. The film thickness was monitored by a quartz crystal during the evaporation. In this project the film thickness was approximately 600~750 nm.

Figure B.8: Thermal evaporation machine [17].

v.   Lift-off

After metal had been evaporated onto the wafers, the samples were transferred to a beaker containing 1-methyl-2-pyrrolidone (NMP-resist stripper). The beaker was placed in a water bath that was pre-heated to $60^{o}C$. The temperature remained constant during the entire process. An important parameter in this process is the time required for the resist stripper to completely remove the resist underneath the metal. It was found out in this project that three hours was sufficient for a clean lift-off.
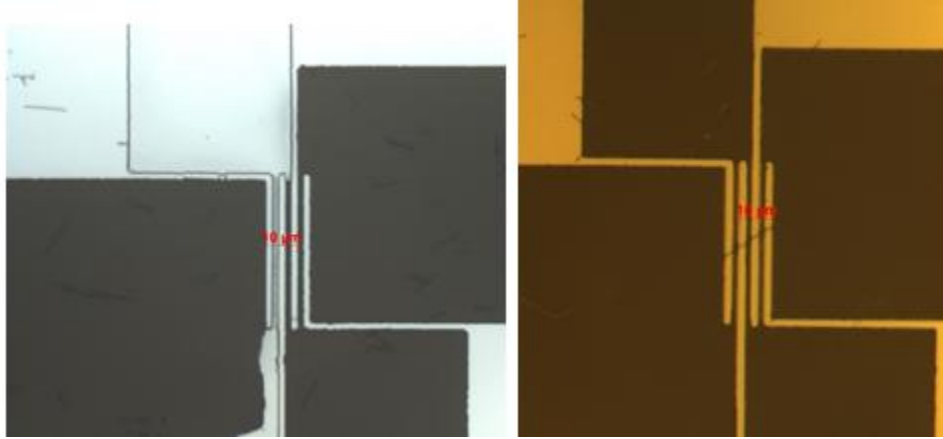

Figure B.9: Left: After one hour, the lift-off is incomplete with silver still remaining on the undesirable areas. Right: after three hours, the lift-off is complete. Notice the nanowire sitting underneath and across the silver fingers that are connected to large measurement pads.